ASR
Insights into the cracking process via lattice fracture simulation at mesoscale based on the chemical reactions at microscale

Qiu, Xiujiao; Chang, Ze; Chen, Jiayi; Schlangen, Erik; Ye, Guang; Schutter, Geert De

DOI
10.1016/j.matdes.2023.111964

Publication date
2023

Document Version
Final published version

Published in
Materials and Design

Citation (APA)
Qiu, X., Chang, Z., Chen, J., Schlangen, E., Ye, G., & Schutter, G. D. (2023). ASR: Insights into the cracking process via lattice fracture simulation at mesoscale based on the chemical reactions at microscale. *Materials and Design*, *231*, Article 111964. https://doi.org/10.1016/j.matdes.2023.111964

Materials & Design 231 (2023) 111964

Contents lists available at ScienceDirect

Materials & Design

journal homepage: www.elsevier.com/locate/matdes

ASR: Insights into the cracking process via lattice fracture simulation at mesoscale based on the chemical reactions at microscale

Xiujiao Qiu [a], Ze Chang [b,*], Jiayi Chen [c], Erik Schlangen [b], Guang Ye [c], Geert De Schutter [a]

[a] Department of Structural Engineering and Building Materials, Ghent University, Ghent 9052, Belgium
[b] Microlab, Faculty of Civil Engineering & Geosciences – Department of Materials & Environment, Delft University of Technology, Delft 2600 AA, The Netherlands
[c] Department of Materials, Mechanics, Management & Design, Delft University of Technology, Delft 2600 AA, The Netherlands

HIGHLIGHTS

- The chemical reaction mechanisms of ASR at microscale and the cracking process at mesoscale in the early stage in concrete without external constraints is linked.
- The cracking process at mesoscale can be divided into four stages.
- Three cracking routes at mesoscale are generalized which can covers various chemical environments at microscale.

GRAPHICAL ABSTRACT

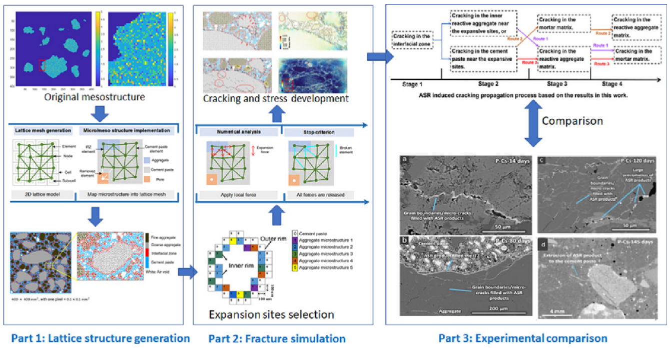

ARTICLE INFO

Article history:
Received 14 November 2022
Revised 22 April 2023
Accepted 25 April 2023
Available online 19 May 2023

2022 MSC:
03

Keywords:
ASR
Multiscale simulation
Cracking development
Chemical reaction
Lattice fracture simulation

ABSTRACT

In our former paper, based on a published 3D reactive transport model at microscale with the capability of simulating the chemical reactions involved in ASR, the location of expansive ASR gel related to the reactivity of aggregate, temperature, aggregate porosity and silica content in aggregate, is clarified. Based on the simulation results, in this paper, the cracking process at mesoscale in concrete induced by ASR in the early stage is investigated. The results show that the cracking process can be divided into four stages and three cracking routes are generalized with the behind chemical exposed environments specified. The cracking routes are found to be comparable with the experimental observed routes. For the first time, the cracking patterns induced by ASR in concrete at mesoscale is linked with the chemical reactions at microscale, which is the first step towards building a complete computational tool to predict ASR as realistic as possible.

1. Introduction

In concrete structures, ASR manifests itself by damaging the structural performance. The reactive aggregate and surrounding cement paste firstly demonstrate mechanical responses such as deformation and cracking caused by the expansive stress induced by ASR products at microscopic level, the cracks are able to then extend to mesoscopic level. With the help of mechanical loading or by gradient of expansion (due to reinforcement or water gradients), ASR is able to cause damaging at structural level. At microscopic level, whether the cracking starts from the surrounding

---

* Corresponding author.
E-mail address: Z.Chang-1@tudelft.nl (Z. Chang).

https://doi.org/10.1016/j.matdes.2023.111964
0264-1275/© 2023 The Author(s). Published by Elsevier Ltd.

cement paste or from the inside of the reactive aggregate varies from aggregate to aggregate.

According to the experimental observations in literature, when the reactive aggregate is non-porous, the initial ASR products are typically observed in the ITZ around the reactive aggregate forming the so-called reaction rim thus lowering the bond between the reactive aggregate and the cement paste [1,2]. While when the aggregate is porous, it is reported that the initial cracking depends on the reactivity of the aggregate [3,4]. As the aggregate is highly-reactive such as volcanic igneous rock, ASR products are also formed in the ITZ [3,4]. As the aggregate is porous and is slowly-reactive such as granitic rock, the initial ASR products tend to be found in the aggregate leading the cracking from the inside of the aggregates [3,4]. For the latter situation, ASR is found to generate gel pockets [5] or gel veinlets [1] or a gel rim surrounding the reactive silica particles inside the aggregate. Alternatively, ions can diffuse into the aggregate through the initial microcracks in the aggregate leading to ASR products formation inside the aggregate too [6,7].

Early ASR fracture simulation models typically only consider the ASR induced cracking in the cement paste, including the definition that aggregate subjected to a compression pressure would not fracture [8–10]. More recent models have realized significant improvements on simulating different cracking patterns. Based on the relationship between the quantitative void and crack content in the aggregate at microscopic level and mechanical measurements at macroscopic level [11], Dunant and Scrivener [12] proposed a model that is able to capture the cracking from the aggregate as well as to predict the mechanical degradation of concrete induced by ASR. In the work of Wang et al. [13], the ASR induced expansion in the ITZ is modelled as an increasing strain in a spring connecting the aggregate and mortar elements. Their work is able to reproduce the cracking network in the cement paste. Both typical expansive sites inside the aggregates or in the ITZ have been considered as a basis in the models of Iskhakov et al. [14] and Miura et al.[15]. In the work of Iskhakov et al. [14], penny cracks were firstly placed inside the aggregate and inside the cement paste. The ASR induced cracking is then modeled by increasing pressure inside those penny cracks. Three expansion models are considered: (1) expansion only inside aggregate leading to cracking inside aggregate; (2) expansion only inside cement paste leading to cracking inside cement paste; (3) expansion inside the aggregate leading to cracking inside the cement paste. The model is able to give the mechanical degradation trend as a function of expansion at concrete level as well as to provide a theoretical upper and lower range that characterize the distribution of the gel in the aggregate or the cement paste for concrete degradation in experiments. In the work of Miura et al. [15], the expansive sites inside the aggregate are modelled as gel pockets randomly placed in the aggregate and the expansive sites in the ITZ are modelled as a reaction rim surrounding the whole aggregate surface. Both 'sharp crack' and 'onion skin crack' observed in [16] were reproduced in the simulation as well as the corresponding cracking processes.

The experimental observations have shown that where the ASR-induced initial cracking starts from (aggregate or cement paste) can be roughly predicted based on the aggregate type or the reactivity of the aggregate. These experimentally observed patterns are used as a basis in the present cracking simulation models at mesoscale. However, there are still many other influential factors that affect the cracking origins such as temperature or the reactive silica distribution etc. More importantly, the link between the chemical reaction mechanism at a lower spatial scale and the produced expansion pressure at mesoscale is not considered in these models. The expansion pressure is calculated and imposed in the aggregate or cement paste either based on assumption or on empirical formula obtained from experimental expansion tests. Moreover, the influence of the change of the expansive sites on the cracking propagation processes induced by ASR is still not fully revealed.

The precise modeling of cracking at aggregate scale induced by ASR requires the information of the chemical reactions at a lower spatial scale. In the previous paper [17], we have simulated different locations of ASR products at microscale by considering different influential factors (reactive silica content in aggregate, alkali concentration, silica microstructural disorder degree and aggregate porosity) in a 3D reactive-transport model with the ability to simulate the chemical process of ASR. Based on these simulation results at microscale, one of the objectives in this paper aims to build a model that can simulate the ASR induced cracking at mesoscale by upscaling these simulation results at microscale to mesoscale so that the gap between the chemical reaction mechanism and the induced physical cracking of ASR can be bridged. Another objective is to compare these different simulated cracking development patterns with the experimental observations and draw a general picture about the ASR induced cracking process with more influential factors, rather than aggregate type, being considered.

2. Modelling approaches

There are multiple simulation tools that can be used to simulate the fracture process of a heterogeneous materials such as finite element analysis (FEM), discrete element method (DEM) or rigid body spring model (RBSM). A multiscale lattice model that is able to simulate the fracture process and the mechanical properties evolution from cement paste to concrete was proposed by Qian et al. [18]. The model is applied by many researches to simulate the cracking and mechanical damage of cement-based materials induced by mechanisms such as shrinkage [19] or sulfate attack [20]. In this study, this lattice model is used to simulate the cracking development in a representative volume element of concrete at mesoscale induced by ASR with the imposed expansive force calculated from the simulated mass of ASR products at microscale in the work of [17]. Compared with the continuum simulation method FEM, the adopted lattice model is able to obtain the cracking progress by removing broken elements one by one. Compared with DEM and RBSM, the differences between are not big except that the adopted model is easier to consider the materials' mesostructure and is more easy to analyse the cracking progress [18].

2.1. Mesostructure generation

The first step of ASR induced fracture simulation is obtaining the microstructure (μm) or mesostructure (mm) of the target materials, which can be obtained either by simulation or by SEM (2D) or CT scan (3D). Considering the computational resources limitation in terms of computer memory and computing time, a 2D mesostructure composed of cement paste, air void, coarse aggregate and fine aggregate in a representative size was generated in this study. The mesostructure is obtained in the following way:

Firstly, a 3D microstructure of concrete composed of cement paste, 3.56% air void in the cement paste, 30% coarse aggregate and 30% fine aggregate with a size of $40 \times 40 \times 40\ mm^3$ with a voxel size of $100 \times 100 \times 100\ \mu m^3$ which is the cubic size of the simulation domain in the chemical simulation model at microscale in the work of [17], was simulated based on the extended model of Chen and Ye [21]. The size of $40 \times 40 \times 40\ mm^3$ was chosen based on the principle [22,23] that the minimum size of a REV of concrete at a mesoscale should be at least 2.5 times bigger than the maximum aggregate size (16 mm in this work). Instead of assuming spherical aggregates, an irregular realistic shape of aggregates is considered in this work based the Anm model from Qian et al. [18] (see Fig. 1(a)). The initial w/c for the cement paste is 0.4 which is consistent to the previous work [17]. The coarse aggregate is assumed to be the reactive siliceous limestone in this paper and its microstructure is composed by five representative simulated 3D microstructures with a size of $100 \times 100 \times 100\ \mu m^3$. In each microstructure, the distribution and the fraction of reactive silica (microcrystalline and cryptocrystalline quartz) and pore is different. More details can be found in the paper [24]. An illustration of the simulated microstructure of coarse aggregates can be viewed in Fig. 1(b) where 1–5 represents the five simulated 3D microstructures of the siliceous limestone.

2.2. Lattice fracture analysis

The next step is then to do the lattice analysis based on the 2D mesostructure. Fig. 2 gives a brief overview of lattice fracture analysis applied in ASR in this work, which includes the lattice mesh generation, microstructure mapping, local force imposing and stop criterion. Each step is further illustrated below.

2.2.1. Lattice mesh generation

In the lattice model, the continuum domain is first divided into s series of cells, in which sub-cells are generated. A lattice node is then randomly placed within each sub-cell which represents solid phase that corresponding to the mesostructure. The pore phase cell does not generate any lattice node. The Delaunay triangulation is adopted to connect the adjacent nodes. Thus the domain is discretized through a series of Timoshenko beams. These lattice beams can transfer the axial force, bending moment and tourqus.

A suitable Poisson's ratio of the structure is realized via changing the size of the cell and sub-cell as shown in Fig. 2. The ratio between the length of sub-cell and cell is defined as randomness which represents the disorder degree of the materials. Simulation in [18] has shown that a value of 0.5 is found to generate a Poisson's ratio of around 0.2 [18], which is close to the Possion's ratio of concrete. In this work, a Possion's ratio of around 0.22 is also reproduced for the meshed structure. Thus, 0.5 is adopted in this work.

2.2.2. Materials mesostructure implementation

A 2D slice of the mesostructure from the 3D obtained mesostructure is randomly selected to map the materials structure into the lattice mesh considering computational burden. Three different beams were generated in this work: aggregate-aggregate elements, cement paste-cement paste elements, interfacial elements that connects the aggregate and the cement paste (20 μm distance of ITZ zone included) The final meshed and mapped lattice network is shown in Fig. 3. The green beam elements represent the interfacial zone. The blue beam elements represent the cement paste and the orange and violet red beam elements represent the aggregates. The pore (air voids) are shown as white.

2.2.3. Element mechanical properties

Table 1 lists the mechanical properties of the involved solid phases, which were used to calculate the mechanical properties for the lattice beam elements. The experimental tested elastic modulus (E) and tensile strength (f_t) of cement paste at microscale from [25] with a size of $100 \times 100 \times 100\ \mu m^3$ and w/c ratio of 0.4, are taken for this study. The shear modulus (G) of cement paste is taken as 0.425 times of E. Following the study of [26,27], the compressive strength (f_c) is 10 times of f_t. The E, G and f_t of the ITZ zone tested through micro-dicing saw and nanoindenter at microscale (with a cement paste size of $100 \times 100 \times 100\ \mu m^3$) in [28] are adopted in this work. Again, the compressive strength (f_c) of the ITZ zone is 10 times of its f_t. For the aggregate, its elastic modulus and compressive strength are 70 GPa and 150 MPa respectively [15,29]. The shear modulus and tensile strength of the aggregate are calculated using the equation $G = 0.425 \times E$ and $f_t = E/1000$ again. The mechanical properties (E, G, f_t and f_c) of a beam element connecting the same phase are equal to that of the local phase. The elastic modulus of an interface element that connects the cement paste and aggregate, are the harmonic average of the elastic modulus [18] as defined below.

$$\frac{2}{E_I} = \frac{1}{E_A} + \frac{0.2}{E_{ITZ}} + \frac{0.8}{E_{CP}} \tag{1}$$

where $E_I, E_A, E_{ITZ}, E_{CP}$ are the elastic modulus of an interface element, aggregate, ITZ and cement paste respectively. The shear modulus of an interface element is determined in a similar way. The tensile or

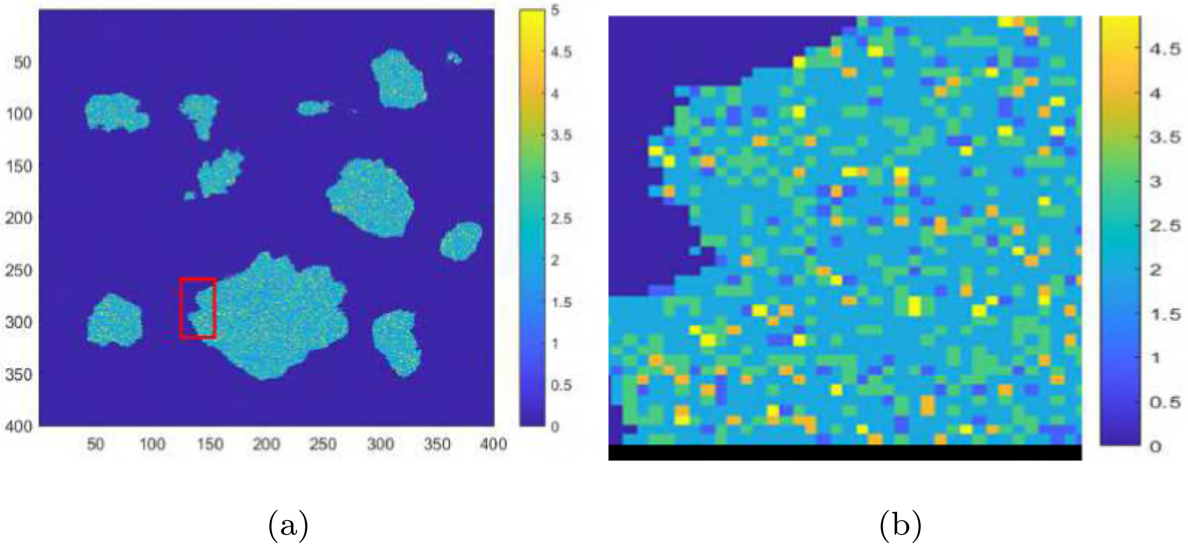

Fig. 1. (**a**): A random 2D slice of the simulated coarse aggregate in cement paste (0); (**b**): Schematic diagram of the microstructure of the part of a coarse aggregate as indicated by the red frame in image (b). 0: mortar; 1–5: the five reconstructed 3D microstructures with a pore and quartz fraction of (0.11%, 6.48%), (0.51%, 10.41%), (0.93%, 20.51%), (1.45%, 32.42%), (2.77%, 40.91%). There are three phases in all microstructures: pore, quartz, and the other inert phases.

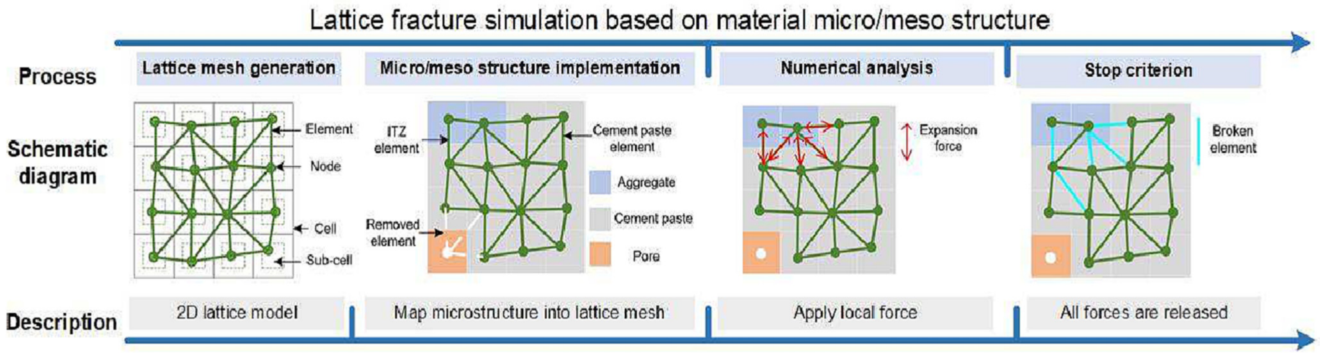

Fig. 2. A brief overview of lattice fracture analysis.

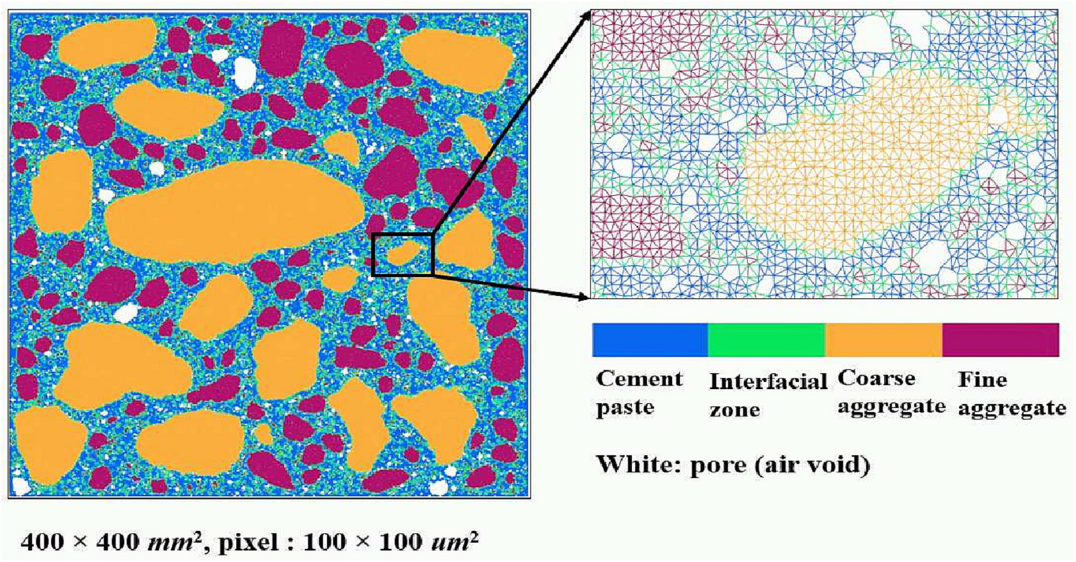

Fig. 3. Left figure: Delaunay triangulation lattice meshes. Right figure shows the zoom of an coarse aggregate and the legend. Here, air voids are the pore with a size bigger than 100 μm.

Table 1
Mechanical properties of different solid phases.

Solid phases	Elastic modulus, GPa	Shear modulus, GPa	Tensile strength, MPa	Compressive strength, MPa
Cement paste	23.41 [25]	9.88	22.71[25]	227.1
ITZ	8.22 [28]	3.49[28]	3.12[28]	31.2
Aggregate	70 [29]	29.75	70	700 [29]

compressive strength of an interface elements is supposed to be the minimum strength among the strengths of the connected solid nodes if the resolution size is smaller than the smallest physical length of solids (ITZ in this work, which is in the range of 10–20 μm) [29,18]. However, in this work, the resolution size is 100 μm which covers the cement past and its surrounding ITZ zone. The strength reduction of an interfacial element due to the exist of ITZ would be lost if the minimum strength is taken. In order to resolve this issue, the same length-weighted harmonic average method is used to determine the tensile strength and compressive strength of an interface element. This method results a strength value of an interface element higher than that of ITZ (lowest) while lower than that of aggregate (highest), which is more realistic.

It should be noticed that the mechanical properties of the solid phases (ITZ, aggregate, cement paste) are taken from literature [27], which were fitted on 3D lattice structure based on the experimental results in [27]. The mechanical properties of the solid phases in a 2D lattice structure are different from that in a 3D structure. Thus, inevitably, the adoption of those values obtained in 3D to a 2D structure will induce deviation. However, the relative mechanical difference between different solid phases are the same whether in a 2D or 3D structure, which is the most important factor relating to the cracking progress which is the main objective of this paper. Therefore, it is reasonable to assume that the adoption of the mechanical strength of ITZ, aggregate and cement paste in 3D to a 2D structure, would not affect the cracking development progress, namely where it will start and to which phase it will develop into. However, the critical expansion force to crack the lattice elements and the cracking patterns in 3D cannot be captured by a 2D simulation.

2.2.4. Local force imposed on lattice elements

In [17], we have utilized a 3D transport-reactive model [30] to simulate the chemical process of ASR at microscale. In the model, the dissolution of silica, the transport of ions, the nucleation and growth of ASR products as well as the transport of the reaction products are numerically simulated. Four representative significant ASR influential factors are studied by using the model including the reactive silica content in aggregate, alkali concentration, silica microstructural disorder degree and aggregate porosity. The influence of the above factors on the chemical reaction sequence, the location of the produced products are investigated. The simulation domain of the model is composed of a cube of cement paste with a size of $100 \times 100 \times 100\ \mu m^3$ and a reactive aggregate cube with a size of $100 \times 100 \times 100\ \mu m^3$. The resolution is $1 \times 1 \times 1\ \mu m^3$. The simulated cement paste microstructure is composed by unhydrated clinker (C_3S, C_2S, C_3A, C_4AF), gypsum, insoluble phases in cement, saturated pores, CH, low density C1.1SH3.9, high density C1.5SH2, aluminate ferrite monosulfate (AFm) and katoite (C_3AH_6). This simulation domain then represents the physical domain of cement paste-aggregate interface in concrete. The dissolution of silica, nucleation and growth of ASR products as well as the dissolution of CH and C-S-H as a buffer effect to ASR are simulated kinetically and thermodynamically with ions diffusion coupled in the transport-reactive model. In the model, three types of non-full nodes are available for ASR products (KSH) to nucleate and grow. Type 1 is the pore nodes. Type 2 is the non-full nodes in the cement paste and type 3 is the partially dissolved silica nodes in the aggregate. When a non-full node becomes full due to KSH formation, the extra KSH is relocated in the surrounding non-full nodes. If there are no more non-full nodes around, the extra KSH then is accumulated at the full node and will cause an increase of the volume. This local volume increase will produce expansive stress in the gel. The relationship between the volume of ASR products and produced pressure can be linked by the gel compressibility as given by Eq. (3) [2]. When the stress exceeds the strength of the surrounding materials, cracking occurs.

$$V_{KSH} = \frac{m_{KSH}}{\rho_{KSH}} \quad (2)$$

$$\Delta P_{asr} = -\frac{1}{\epsilon_{KSH}} ln \frac{V_0}{V_{KSH}} \quad (3)$$

$$f_{asr} = \Delta P_{asr} \times a_{cell} \quad (4)$$

where V_{KSH} (m^3) is the total volume of the produced KSH in a local lattice node (with a size of $100 \times 100 \times 100\ \mu m^3$), m_{KSH} is the corresponding mass of KSH. $V_0 = V_{KSH} - \Delta V_{KSH}$ (m^3) is the volume of KSH that can be accommodated in the node with ΔV_{KSH} being the extra KSH volume in that node. ρ_{KSH} (kg/m^3) is the density of KSH. In the work of Dunant [5], about 50 % volume expansion of ASR products was found to fit the experimental data, which means for the same mass, the volume of ASR product equals to 1.5 times volume of the original silica. Therefore, 2/3 of the density of silica (1.77 g/cm^3) was used for KSH. ΔP_{asr} (Pa) is the produced pressure in the node by the extra KSH, and ϵ_{KSH} (Pa^{-1}) is the compressibility of KSH. For condensed inorganic materials, it lies between 10^{-11} Pa^{-1} - 10^{-10} Pa^{-1}, and 10^{-10} Pa^{-1} is adopted in this work [2]. f_{asr} (N) is the corresponding expansive force produced in the local lattice node and a_{cell} is the cross-section area of a voxel, which is $0.1 \times 0.1 \times 10^{-6}\ m^2$.

In the lattice model at mesoscale, the resolution becomes $100 \times 100 \times 100\ \mu m^3$, which means the cement paste or aggregate cube simulated at microscale now becomes a node at mesoscale. The calculated expansive forces f_{asr} in the cement paste cube and the aggregate cube at microscale are then imposed on the lattice elements that connect the cement paste nodes surrounding the coarse aggregate and on the lattice elements that connect the coarse aggregate surface nodes respectively. As shown in Fig. 4(a), a 2D lattice node 0 is surrounded by eight nodes represented by 1 to 8, resulting in maximum 8 lattice elements. However, the true number of elements depends on the final meshed structure and a minimum of 4 connected lattice elements is found for each node. The expansive forces are then distributed on the lattice elements $0-1, 0-2, 0-3$ and $0-4$ as shown by the yellow elements in Fig. 4(a), as the corresponding surrounding nodes 1, 2, 3 and 4 which represent a cell respectively have the biggest contact area with the expansive node 0. One may chose to distribute the forces on more than 4 elements connected to the expansive node, but it should be aware that more balance equations (stated later) are then needed and the solution may not convergent depending on the number and coordinates of the selected elements. Furthermore, the area used in Eq. 4 to calculate the forces imposed on other elements ($0-5, 0-6, 0-7$ and $0-8$) should also be adjusted since the contact area with the expansive node is not a_{cell} anymore. In this work, these elements are not taken into con-

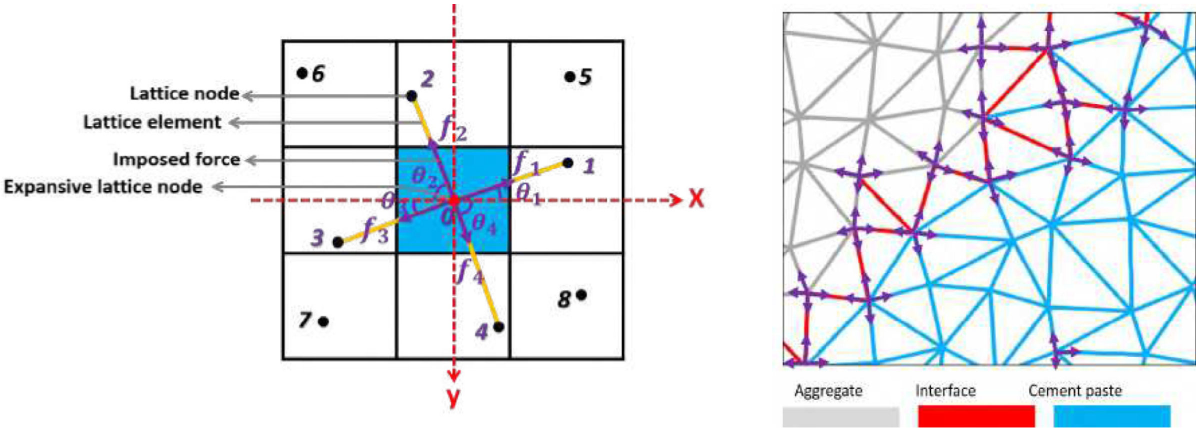

(a) (b)

Fig. 4. (**a**): A schematic diagram for the method for imposing ASR-induced forces on lattice elements. (**b**): A schematic diagram for the imposed local force on lattice elements.

sideration for simplification. But it would not cause big difference as the distributed forces on elements $0-5, 0-6, 0-7$ and $0-8$ should be much less than those on elements $0-1, 0-2, 0-3$ and $0-4$.

The final imposed force on each lattice element is defined as f_1, f_2, f_3, f_4 as shown by the purple arrow in Fig. 4(a). These four forces are then calculated by solving the four balance equations (Eq. (5) to Eq. (8)), where $\theta_1, \theta_2, \theta_3, \theta_4$ are the angle between each lattice element $(0-1, 0-2, 0-3)$ and X axis, which are calculated according to the node coordinates.

$$f_1 \times \cos\theta_1 + f_2 \times \cos\theta_2 + f_3 \times \cos\theta_3 + f_4 \times \cos\theta_4 = 0 \tag{5}$$

$$f_1 \times \sin\theta_1 + f_2 \times \sin\theta_2 + f_3 \times \sin\theta_3 + f_4 \times \sin\theta_4 = 0 \tag{6}$$

$$f_1 \times \cos\theta_1 + f_4 \times \cos\theta_4 = f_{asr} \tag{7}$$

$$f_2 \times \cos\theta_1 + f_3 \times \cos\theta_4 = -f_{asr} \tag{8}$$

Eq. (5) and Eq. (6) represent the force balance at X axis and Y axis respectively, while Eq. (7) and (8) represent that the sum of the component forces in the positive and negative directions of the X axis are f_{asr} and $-f_{asr}$ respectively. It should be noticed that after meshing the structure, not every expansive node is connected to its node 1 to node 4. Some of the nodes are only connected with two of these nodes such as node 1 and node 3 or three of them. Thus, the number of above equations decreased to two or three or the imposed forces decreased to two or three. It is also possible that a node possesses only lattice element $0-1$ and $0-4$ or $0-2$ and $0-3$, for which no solution for the above equations can be found. For these expansive nodes, they are excluded from the system. Our study shows that in the following simulation, about 1% of the expansive nodes are excluded.

At mesoscale, the calculated force f_{asr} was then imposed as a compressive force on the lattice element as shown in Fig. 4(b). It should be noted that in this schematic diagram, ASR induced forces are only imposed on the surface of the aggregate element, on the interface elements and on the cement paste elements connecting to the aggregate surface, since the input are taken from [30] where the chemical reactions simulated are limited between the cement paste and aggregate surface. This will induce discrepancies from some realistic situations, such as pore solution ions can diffuse into the very inside of the aggregate if the aggregate is highly porous or there are initial defects in the aggregate. These aspects will be further discussed in the next section.

2.2.5. Failure criterion

In the lattice fracture analysis, the calculated compressive forces are imposed on the system as a force increment step by step. At each analysis step, a critical lattice element and a system scaling factor are determined. More computation details can be found in [31]. The critical lattice element is the one with the highest stress/strength ratio. The system scaling factor is the inverse of the ratio. This scaling ratio, together with a constant reference force defined in the fracture model, determine the imposed force increment in the next analysis step to make sure that only one element will be broken in the system. The critical lattice element is then removed from the system and if the sum of the imposed force at each lattice element does not reach its target force (the calculated compressive force), the analysis is repeated. The step-by-step removal of critical lattice elements indicates the cracking evolution and the reaction kinetic of ASR in the system.

It should be noticed that for some lattice elements where the compressive forces are imposed, it is possible that these elements are broken before the imposed forces reach the target ones. For this situation, no further forces are imposed on these elements since they are removed from the system. In the real situation, after cracking, ASR products can be formed in the formed cracks and further induce damage. However, in this study, the cracking is not coupled in the chemical reaction model meaning that further chemical reactions in the formed cracks are not considered thus only the initial cracking propagation induced by ASR products in the early stage can be obtained.

2.3. ASR expansion models

2.3.1. Similarities and discrepancies between the simulated expansive sites and observed ones

In this section, different ASR expansion models will be determined which can represent the typical initial expansive sites at mesoscale based on the chemical reaction simulation results at microscale as well as the experimentally observed locations of expansive sites induced by ASR. As aforementioned, there are some discrepancies between the simulation results (location of ASR products) in [17] and some experimentally observed ones. A brief summary of the simulated initial ASR products location at microscale in [17] are revisited as well as the field situations that are not captured by the 3D reactive-transport lattice simulation model.

Three typical different locations of ASR products, namely inside aggregate, inside ITZ and cement paste, and inside aggregate, ITZ and cement paste, are reproduced in [17] by studying the influence of reactive silica content in aggregate, alkali concentration, silica microstructural disorder degree and aggregate porosity on ASR in the early stage. It was found that the location of ASR products is not affected by the initial alkali concentration in pore solution, while it is significantly affected by the other factors. For more details, one can refer to [17]. Based on the simulation results, two summarized ASR product location instruction diagrams are shown in Fig. 5 (temperature is also included which is not stated in [17]). It can be seen that with a temperature of 25 °C and a low aggregate porosity of 0.24%, the location of the initial ASR products in the aggregate can be anticipated when the aggregate is slowly reacting (the silica dissolution activation energy $E_a = 78$ $\text{KJ} \cdot \text{mol}^{-1}$). However, when the aggregate porosity increases, the initial location changes with the reactive silica fractions in the aggregate while the other parameters are the same. When its reactive silica fraction is higher than 20.51%, with an aggregate porosity of 0.8%, the location of the initial ASR products in ITZ and cement paste can be anticipated. The initial ASR products inside the aggregate are only possible when the reactive silica fraction is lower than 10.41%. Nevertheless, this turning reactive silica fraction decreases with the aggregate porosity increasing. When the temperature is as high as 80 °C or the aggregate is highly-reactive ($E_a = 60$ $\text{KJ} \cdot \text{mol}^{-1}$), ASR products are formed inside ITZ and cement paste regardless of other factors. However, when the aggregate porosity is as high as 4.88%, no matter how high the reactive silica fraction or the temperature or the reactivity of the aggregate is, ASR products tend to be formed both inside aggregate and cement paste. Similarly, this turning porosity decreases as the reactive silica fraction increases.

As can be seen, a simulation model at microscale was built, which is able to simulate the chemical reaction process of ASR and it was utilized to simulate the influence of reactive silica content in aggregate, alkali concentration, silica microstructural disorder degree and aggregate porosity. The outputs are the location and amount of the chemical reaction products under these designed different chemical environments. However, one of the limitation of the model is that the reaction is limited at the cement paste-aggregate. This is consistent to what have been found in experiments, if the aggregate porosity is so low that the reaction can only happen at the interface. However, if the aggregate porosity is very high, ions can diffuse into aggregate much further than the simulated distance (100 μm) [7] or there are some initial cracks in the aggregate, the ions can diffuse into the very inside of the

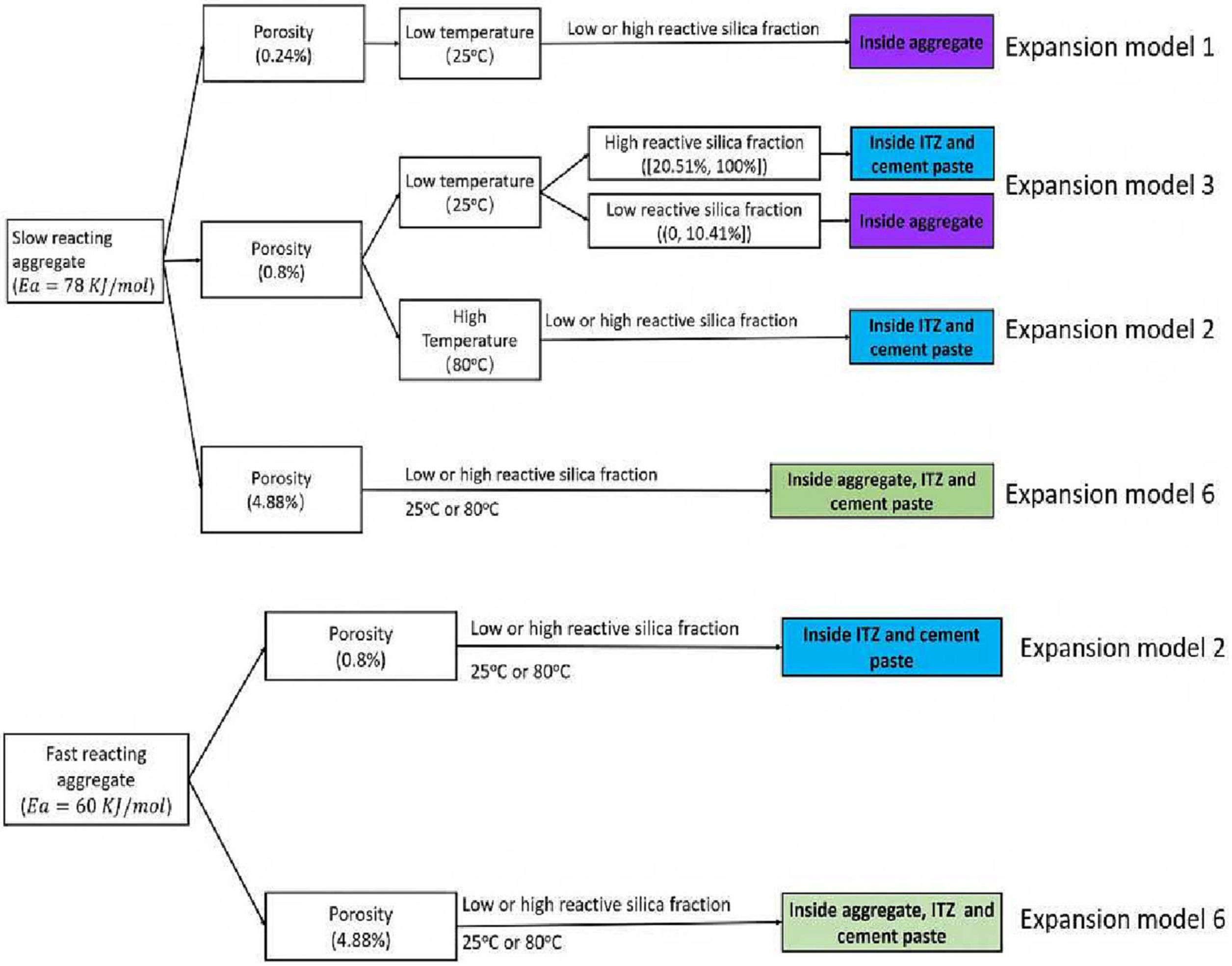

Fig. 5. Instruction diagrams of location of ASR expansive products considering the influence of the reactive silica content, the silica microstructural disorder degree, temperature and aggregate porosity for two kinds of reactive aggregate.

aggregates and trigger ASR there as can be seen in Fig. 22(b), which cannot be captured by the microscale model.

As the main objective of this work is to give insights about the initial cracking progress in concrete induced by ASR, we have also considered the above situation where ASR is triggered inside the aggregate when the porosity is high or there are initial cracks, which is discussed in the next section.

2.3.2. Typical ASR expansion models

Fig. 6 shows a 2D schematic diagram for the chemical reaction front of ASR that is simulated at microscale. The reaction front is divided into an inner rim and an outer rim. As shown in the figure, the inner rim is the coarse aggregate surface layer with a thickness of 100 μm, while the outer rim is the cement paste layer with a thickness of 100 μm surrounding the coarse aggregate. Based on the above syntheses of the chemical reaction simulation results of ASR at microscale, six ASR expansion models that can represent various chemical environments are used in this work to study the cracking patterns.

- Expansion model 1: Expansive sites locate at the inner rim;
- Expansion model 2: Expansive sites locate at the outer rim;
- Expansion model 3: Expansive sites locate at both inner rim and outer rim with higher expansive force in the outer rim;
- Expansion model 4: Expansive sites locate at both inner rim and outer rim with higher expansive force in the inner rim;
- Expansion model 5: Expansive sites locate at the inner rim and randomly inside the aggregate as shown in Fig. 7 (a);
- Expansion model 6: Expansive sites locate at a wider layer including the inner rim as shown in Fig. 7 (b).

The expansion model 1 accounts for the case that the initial ASR products are only formed inside the reactive aggregate at the surface in concrete when the aggregate porosity is very low and the temperature is low (below 25 °C) or when the aggregate is slowly reactive with a low porosity and small reactive silica fraction at a low temperature as shown in Fig. 5. For this expansion model, five chemical reaction simulations $[D_{71}, D_{72}, D_{73}, D_{74}, D_{75}]$ at microscale are done with the parameter settings shown in Table 2. The initial calcium concentration is set to be 2 $mmol \cdot L^{-1}$ and the initial alkali concentration is 0.75 $mol \cdot L^{-1}$ which are realistic values in the pore solution of concrete. The aggregate is slowly reactive with a porosity of 0.24% and the silica fraction distributions at aggregate cubes are 6.58%, 10.41%, 20.51%, 32.41% and 40.91% respectively. The temperature is 25 °C. The simulation results from systems $[D_{71}, D_{72}, D_{73}, D_{74}, D_{75}]$ are then used to calculate the ASR-induced forces based on Eq. (2)–(4). The calculated forces are then imposed on the lattice elements as described before.

The expansion model 2 accounts for the case that the initial ASR products are only formed inside the cement paste that surrounds the reactive aggregate such as when the aggregate is highly reac-

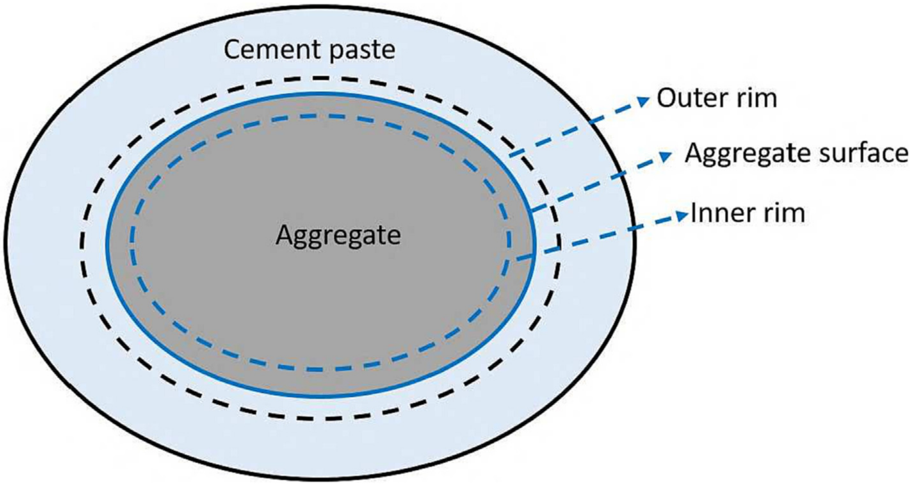

Fig. 6. Schematic diagram for the simulated chemical reaction fronts at microscale.

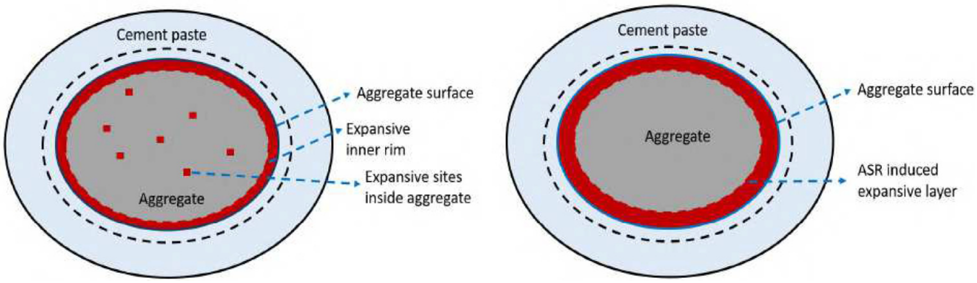

(a) (b)

Fig. 7. Schematic diagrams of expansion model 5 (**a**) and expansion model 6 (**b**).

Table 2
Summary of the simulation parameter settings.

Simulation system ID	**Reactive silica content in aggregate, %**	$\mathbf{K^{+}_{eq}}$ [a], $mol \cdot L^{-1}$	E_a [b], $J \cdot mol^{-1}$	ϕ_{agg} [c], **%**	$\mathbf{Ca^{2+}}$ [d], $mol \cdot L^{-1}$
$[A_{31}, A_{32}, A_{33}, A_{34}, A_{35}]$ [e]	[6.58 10.41 20.15 32.41 40.91]	0.75	78000	0.8%	0.02
$[R_{41}, R_{42}, R_{43}, R_{44}, R_{45}]$	[6.58 10.41 20.15 32.41 40.91]	0.75	60000	0.8%	0.02
$[D_{11}, D_{12}, D_{13}, D_{14}, D_{15}]$	[6.58 10.41 20.15 32.41 40.91]	0.20	78000	10.38%	0.02
$[D_{71}, D_{72}, D_{73}, D_{74}, D_{75}]$	[6.58 10.41 20.15 32.41 40.91]	0.75	78000	0.24%	0.002

a: The initial concentration of K^{+}_{eq} in the system, equals to the sum of Na^{+} and K^{+} concentration. b: The activation energy of silica, represents the reactivity of silica. c: The porosity of coarse aggregate. d: The initial Ca^{2+} concentration in the system. e: In systems $[A_{31}, A_{32}, A_{33}, A_{34}, A_{35}]$, the difference is the reactive silica content in aggregate which is 6.58%, 10.41%, 20.51%, 32.41%, 40.91% respectively. The same principle applies to other simulation identities (IDs). For all systems, the temperature is 25 °C.

tive or the temperature is very high (for example, higher than 80 °C) as shown in Fig. 5. The simulation results from system $[R_{41}, R_{42}, R_{43}, R_{44}, R_{45}]$ are used in this model to calculate the compressive forces and then imposed on the interfacial lattice elements that connect cement paste surrounding the reactive aggregate. More details about the parameter settings about the systems can be found in Table 2, which are not repeated here again.

The expansion model 3 accounts for the case that when the temperature is low (below 25 °C) and the aggregate porosity is low, the reactive silica distribution is heterogeneous at the surface so that the ASR products are formed inside the aggregate where the local reactive silica content is low, while in the surrounding cement paste where the local reactive silica content is high as shown in Fig. 5. The simulation results from systems $[A_{31}, A_{32}, A_{33}, A_{34}, A_{35}]$ are used to calculate the compressive force in this model (see Table 2). In system $[A_{31}, A_{32}]$, the initial expansive sites are inside the aggregate, while in system $[A_{33}, A_{34}, A_{35}]$, the initial expansive sites are in the ITZ and cement paste. Due to high silica fraction in the systems $[A_{33}, A_{34}, A_{35}]$, the calculated compressive forces inside the cement paste are higher than that in the aggregate.

The expansion model 4 accounts for the case that ASR products are generated inside the aggregate and cement paste but the resulting force inside the aggregate is higher than that in the cement paste. This expansion model and the expansion model 3 are in contrast. By comparing the results, it is possible to obtain the influence of the relative ASR-induced force magnitude between the aggregate and the cement paste on the cracking process. However, such a distribution of induced forces is not simulated at microscale. Thus, the calculated compressive forces in the expansion model 3 are imposed in this model with the change that the average force in the inner rim is higher than that in the outer rim.

The expansion model 5 accounts for the case where the low or non-porous aggregate has initial defects inside the aggregate but heterogeneous distributed. 1.25% expansive sites are randomly placed inside the aggregate except the inner rim. Then a compressive force higher than a cracking trigger force is imposed on the random expansive sites inside the aggregate. According to our simulation results, the expansive pressure should be higher than around 4×10^6 Pa for the cracking to start. Simulations with 0.3%, 0.8% and 1.0% expansive sites are also done. It is observed that the qualitative results are as same as that of 1.25% expansive sites.

The expansion model 6 accounts for the case when the aggregate porosity is very high as shown in Fig. 5 such as light weight aggregate so that the inner rim is actually more than 100 μm. Thus, a layer from the aggregate surface within a distance of around 1 mm is assumed to expansive as indicated in Fig. 7 (b). The simulation results from system $[D_{11}, D_{12}, D_{13}, D_{14}, D_{15}]$ (more inputted chemical parameters can be found in Table 2) are used to calculate the compressive forces in the outer rim and inner rim. The compressive forces in the layer further than 100 μm is then taken as the values of the compressive force of the inner rim with a linear decrease as a function of distance. The calculated compressive force in the lattice node in the inner rim (zone with a distance of 0.1 mm to the aggregate surface) is defined as f_{asr}. With a distance of x mm to the inner rim, the compressive force $f_{(x)}$ is then calculated by the equation $f_{(x)} = f_{asr} - f_{asr} \times \frac{x}{0.9}$ as shown in Fig. 8. This is an assumption based on the fact that as the distance from the aggregate surface increases, ions concentration decreases due to the consumption by ASR. Even though the assumption is a simplification, it is able to give insight about the cracking process in this case.

In this work, the distribution of the ASR-induced forces, which is calculated based on the results in [17], in the aggregate lattice nodes is heterogeneous depending on the local reactive silica concentration. This is more realistic compared with the present simulation models in which the expansive forces are the same at the assumed expansive sites. No mechanical boundary conditions are applied in all of the models, which means that the structure is expanded freely. However, in field, concrete structures are normally under constraint. ASR expansions were found to be reduced by the external compressive constraint [32,33] and the cracking were promoted in a direction perpendicular to the restraining direction [34]. By applying the free expansion boundary condition, the influence of boundary constraint on the cracking development is excluded. Thus, the pure influence of ASR on the initial cracking process is evaluated in this work, which can be further used to study the coupling effect of external constraints.

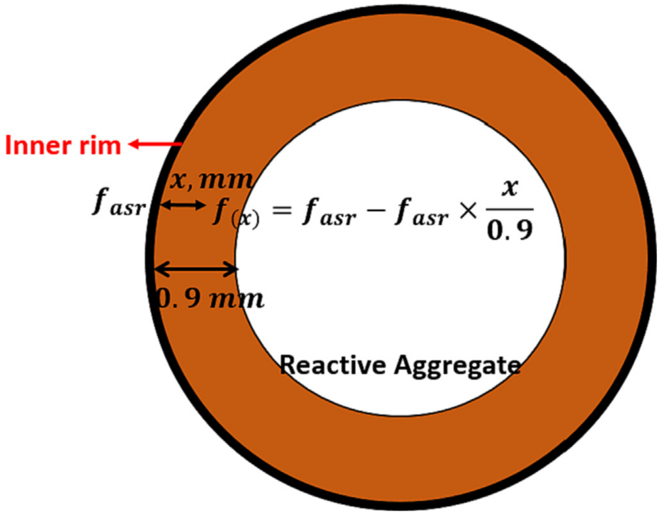

Fig. 8. Schematic diagrams of the calculation method for the ASR-induced forces in the layer from 100 μm to 1 mm to the aggregate surface in the expansion model 6.

3. Modelling results

3.1. Expansion model 1

As aforementioned, in this expansion model, the expansive sites are heterogeneously distributed in the inner rim. The calculated pressures from $[D_{71}, D_{72}, D_{73}, D_{74}, D_{75}]$ based on the formed amount of KSH in each system at the same time are taken (see Table 2). The calculated expansive pressure are in the range of $[10^6, 10^8]$ Pa.

Fig. 9 shows the cracked elements at different analysis steps in a small reactive aggregate and part of a big reactive aggregate resulted from model 1. The small and big aggregate are chosen to give a clear illustration about the locations of the developed cracks. It was also found that the cracking development and stress development in/and around the chosen small and big aggregate are representative for the cracking and stress development in the structure. The black line represents the element that is broken. It can be seen that after 300 steps, initial cracking occurs in the interfacial zone since the mechanical strength there is the lowest. With analysis on going, more elements in the interfacial zone are broken (Fig. 9(b)). Then cracking inside the reactive aggregate occurs (as shown by the red arrows in Fig. 9(c)). The cracks are near the surface in both small and big aggregate and the cracks inside the small reactive aggregate are more obvious than that in the big reactive aggregate. After that, cracking in the cement paste is also observed as shown by the red circle in Fig. 9(d). In the end, the reactive aggregates are debonded from the cement paste and the reactive coarse aggregate interior near the surface are damaged with the small reactive aggregate being more severe. Cement paste is damaged as well. The cracking inside the fine aggregate is not found yet in this expansion model, but cracks near the fine aggregate boundary and cracks connect two close aggregate are formed as can be seen in Fig. 9(d).

Fig. 10 shows the tensile stress (positive value) and compressive stress (negative value) developments in the same small aggregate and part of a big aggregate. The dark line as indicated by the blue arrow in Fig. 10(a) represents the interfacial element, which gives the outline of the aggregates. Fig. 10(a) indicates that after 300 analysis steps, tensile and compressive stress are mainly generated in the interfacial elements along the peripheral of the reactive aggregate as well as inside the reactive aggregates but near the interfacial surface. The stresses keep increasing (Fig. 10(b)) and propagate towards the inside of the reactive aggregate as well as towards the mortar matrix. After 4000 steps, tensile stress in the non-reactive fine aggregate becomes obvious as shown by the red circle in Fig. 10(c). The propagation of the compressive stress is not as far as tensile stress and is limited around the reactive aggregate surface. But as cracking going on, its value increases to be the dominant stress in the reactive aggregate in the end. During the whole analysis process, most of the highest tensile and compressive stress appears at the aggregate-cement paste interface and inside the aggregate near to the boundary.

The above analyses indicate that in the expansion model 1 where the initial expansive sites are heterogeneously distributed at the aggregate surface and the ASR generated pressure is in the range $[10^6, 10^8]$ Pa, cracking first appears in the aggregate-cement paste interface, developing along the expansive sites at the surface boundary of the reactive aggregate and extends into the reactive aggregate near the aggregate-cement paste interface. After that, cracking in the cement paste happens. By checking the cracking mechanism of every broken element, which is one of the output of the simulation results, it is found that 6317 elements

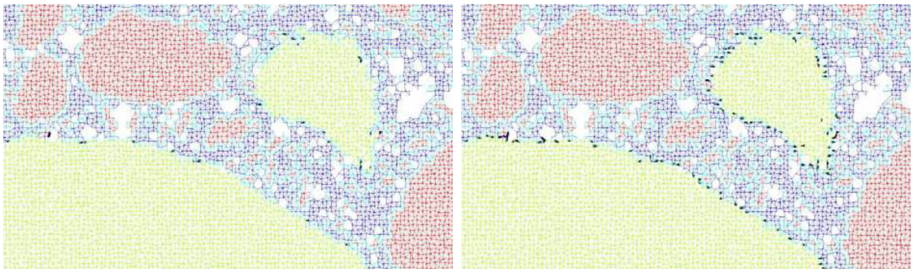

(a) Step 300 (b) Step 2000

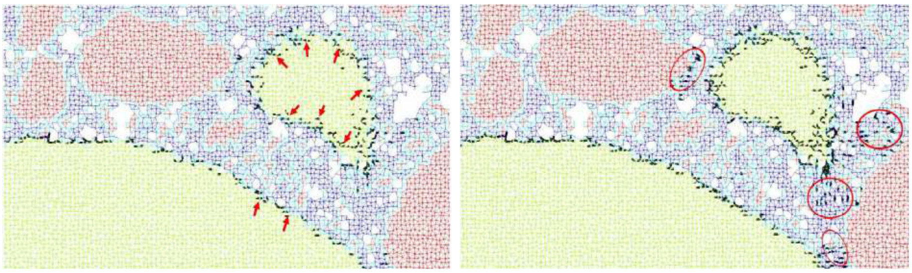

(c) Step 4000 (d) Final step

Fig. 9. Illustration of cracking development in the expansion model 1 at different analysis steps. The black line represents the broken element.

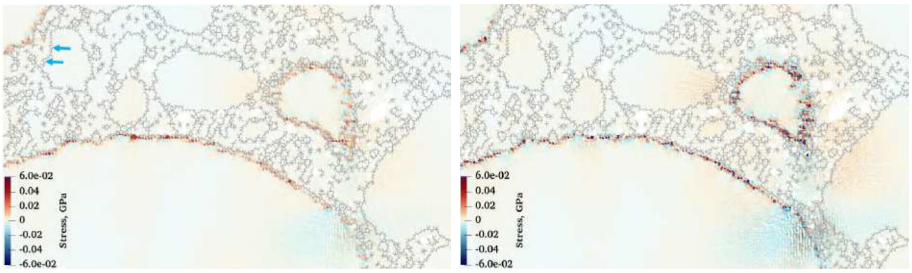

(a) Step 300 (b) Step 2000

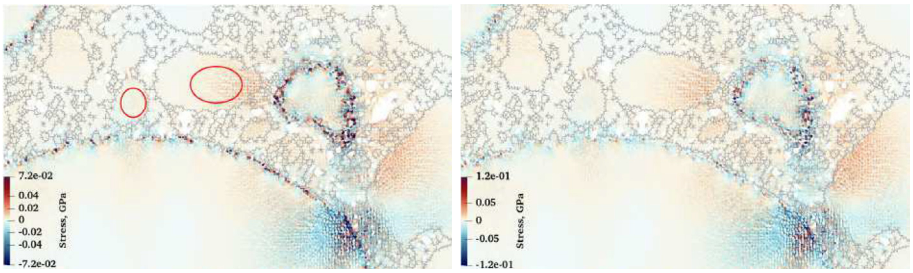

(c) Step 4000 (d) Final step

Fig. 10. Illustration of stress development in the expansion model 1 at different analysis steps. The dark line represents the interfacial element, which gives the outline of the aggregates. Red circle indicates the propagation of tensile stress into the fine aggregate.

are broken due to the local tensile stress failure, and no element is broken due to compressive stress failure. According to the tensile stress distribution in the end (Fig. 10(d)), cracking inside the fine aggregate can be expected if the expansive force is high enough.

3.2. Expansion model 2

In this expansion model, the expansive sites are distributed in the outer rim. The calculated expansive pressures from $[R_{41}, R_{42}, R_{43}, R_{44}, R_{45}]$ (see Table 2) are taken. The calculated pressure is in the range $[10^7, 10^8]$ Pa. Similar to Fig. 9, Fig. 11 shows the cracked elements at different analysis step in a small reactive aggregate and part of a big reactive aggregate. Again, it can be seen that elements in the interfacial zone are firstly broken (Fig. 11(a)) but then the cracking extends towards the cement paste around the aggregate as shown in Fig. 11(b), Fig. 11(c) and Fig. 11(d), which is different from the pattern in the expansion model 1. In the end, the reactive aggregates are debonded from the cement

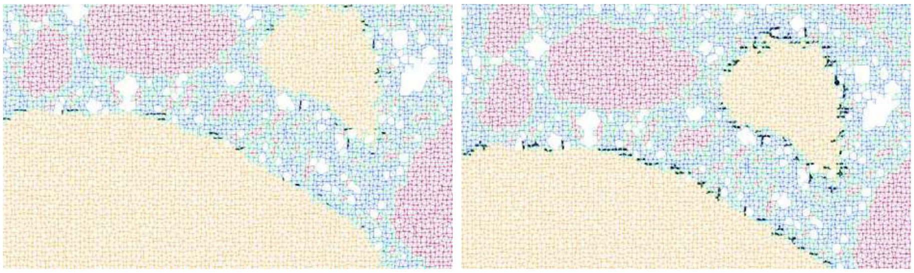

(a) Step 1000 (b) Step 3000

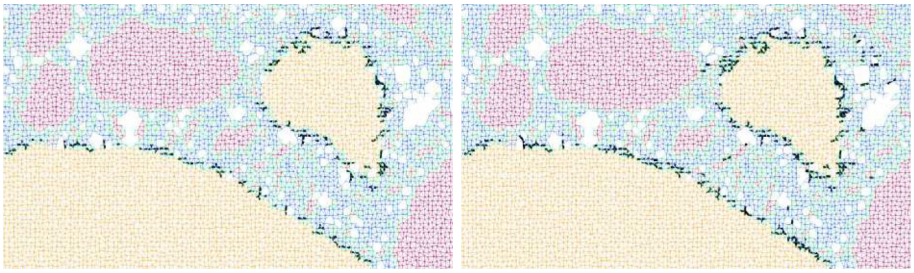

(c) Step 5000 (d) Final step

Fig. 11. Illustration of cracking development in the expansion model 2 at different analysis steps.

paste. A cracking network in the cement paste and cracking inside the fine aggregate are not observed either in this expansion model.

The stress development in Fig. 12 illustrates that after 300 steps, both tensile and compressive stresses are generated around the expansive sites which are mainly in the interfacial zone, the near cement paste zone and reactive aggregate interior in a limited distance (Fig. 12(a)). The stress keeps increasing with increasing analysis steps with the highest stresses always at the interfacial elements and in the cement paste near the aggregate-cement paste interface. With steps increasing, the tensile stresses propagate towards both the aggregate interior and the mortar matrix. In the end, tensile stresses propagated in the non-reactive fine aggregates close to the reactive aggregates can be obviously found as shown by the red circles in Fig. 12(c) and Fig. 12(d). The compressive stress is mainly generated around the expansive sites near aggregate surface, increasing and extending mainly into the cement paste as the cracking going on, but in a limited distance compared with the propagation of tensile stress as can be seen by the blue area in Fig. 12(d).

The above analyses indicate that in the expansion model 2 where the initial expansive sites are distributed at cement paste including ITZ near the aggregate surface and the ASR generated

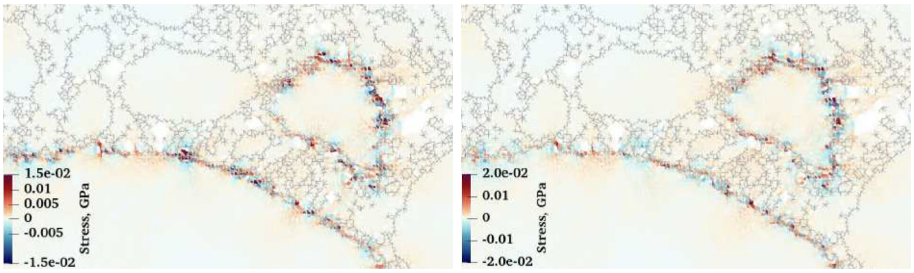

(a) Step 300 (b) Step 1000

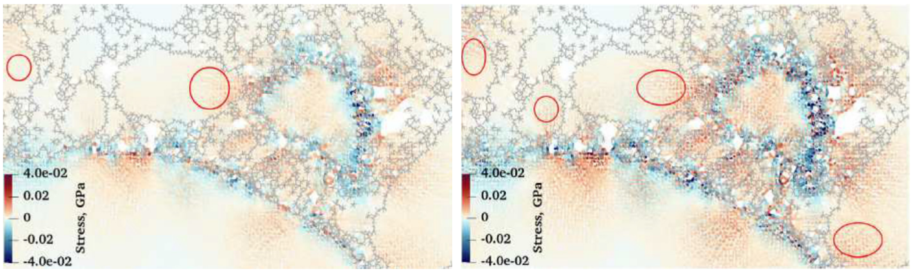

(c) Step 4000 (d) Final step

Fig. 12. Illustration of stress development in the expansion model 2 at different analysis steps. The dark line represents the interfacial element, which gives the outline of the aggregates. Red circle indicates the propagation of tensile stress into the fine aggregate.

pressure is in the range $[10^7, 10^8]$ Pa, cracking first appears in the reactive aggregate-cement paste interface, developing along the expansive sites at the surface boundary of the reactive aggregate and then extends into cement paste near the aggregate-cement paste interface. 6136 elements are broken due to the local tensile stress failure, and no element is broken due to compressive stress failure. Similarly, according to the tensile stress distribution in the end, cracking inside the aggregates as well as a crack network can also be expected if the expansive force is high enough.

3.3. Expansion model 3 and Expansion model 4

In the expansion model 3, the expansive sites are heterogeneously distributed both in the inner rim and outer rim. The calculated pressures from $[A_{31}, A_{32}, A_{33}, A_{34}, A_{35}]$ (see Table 2) are taken. The expansive pressure is in the range $[10^6, 10^{10}]$ Pa with a higher pressure located inside the cement paste node that connects to the aggregate node with a high silica fraction ($[A_{34}, A_{35}]$).

Similarly, initial cracking starts from the interfacial zone as shown by Fig. 13(a). However, the cracks along the interface are very concentrated at the expansive sites and are not connected as in the model 1 and model 2, because the lowest pressure 10^6 Pa in some expansive sites is not high enough to break any elements. After that, cracks are formed inside the mortar matrix as can be seen from the red circle in Fig. 13(c). It can also be seen that part of the non-reactive fine aggregates are partly debonded from the cement paste. Cracks inside the coarse aggregate is not observed, probably because the imposed stress is not large enough. In the end, fine aggregates are connected by cracks and the cement paste is severe damaged.

Fig. 14 shows the stress development in this model. In the beginning, stress is generated at and around the expansive sites and extends to few sites in the cement paste and in the reactive aggregate near the expansive sites as shown by Fig. 14(a). Very soon, small compressive stresses are generated in the structure (Fig. 14(b)) and it propagates into most of the area of the structure as shown in Fig. 14(c). In the end, as shown by Fig. 14(d), the compressive stress becomes dominant and are distributed in most of place of the structure in the interior while the tensile stress is distributed at the exterior of the structure, at the aggregate boundaries and at a small part inside the aggregates. This means that when the input stress is large, further development of compressive stress through the whole materials can be observed, which can also be observed in the expansion model 6 (Fig. 19(f)). By checking the cracking mechanism, it is found that in the beginning, the cracking is caused mainly by tensile failure. After that, cracking the caused by compressive failure also occurs. In total, 4228 elements are broken due to the local tensile stress failure, and 1300 elements are broken due to compressive stress failure. This means that the cracking mechanism can be induced both by tensile and compressive strength failure, but the latter one only happens when the induced expansive pressure is very high such as 10^{10} Pa.

This expansion model is a combination of the expansion model 1 and 2 except that the expansive forces inside the cement paste are much higher than that in the expansion model 2. The above three models indicate that after cracking inside the interfacial zone, it propagates firstly towards where the expansive forces are higher. In order to further validate this observation, an expansion model (model 4) will be analyzed in which the expansive sites are distributed in the inner rim and outer rim but the forces in the inner rim are higher. The expansive pressure is in the range $[10^6, 10^{10}]$ Pa with the higher pressure locating in the aggregate. The cracking development in Fig. 15 shows that the cracking in this model firstly happens in the interfacial zone and then extends into the reactive aggregate near the expansive sites as shown by the red arrows in Fig. 15(b) and Fig. 15(c), after that, cracks inside cement paste are developed as indicated by the yellow circle in Fig. 15(d). In total, 4228 elements are broken due to the local tensile stress failure, and 1300 elements are broken due to compressive stress failure. The cracking process in this model has confirmed the stated observation that cracks propagate towards where the expansive forces are higher.

3.4. Expansion model 5

In this expansion model, the expansive sites are distributed in the inner rim and inside the reactive aggregate (1.25% of random expansive nodes) to represent the realistic situation that ions can diffuse into the low or non-porous aggregate through the initial defects inside the aggregate which are either produced via geological activities or crushing operations. Similar to the expansion model 1, the calculated pressures from $[D_{71}, D_{72}, D_{73}, D_{74}, D_{75}]$ are taken.

The only difference between this expansion model and the expansion model 1 is the random expansive sites in the aggregate interior. Thus, the cracking pattern in the early analysis stage is similar to that in the expansion model 1 showing that cracking starts from the breaking of the elements in the interfacial zone (Fig. 15(a)) and then propagates towards the aggregate interior near the surface as can be seen in the small aggregate shown by the red arrows in Fig. 16(b). After that, cracks inside the aggregate near the random expansive sites are generated as shown by the red circle in Fig. 16(c). In the later stage, cracking in the cement paste is observed as illustrated by the yellow circle in Fig. 16(d). However, a crack network inside the reactive aggregate as well as in the cement paste is not observed yet. Again, it is probably because the generated expansive force is not high enough.

The stress development in Fig. 17 shows that in the beginning, both tensile stress and compressive stress are generated at and near the interfacial zone and the expansive sites inside the coarse

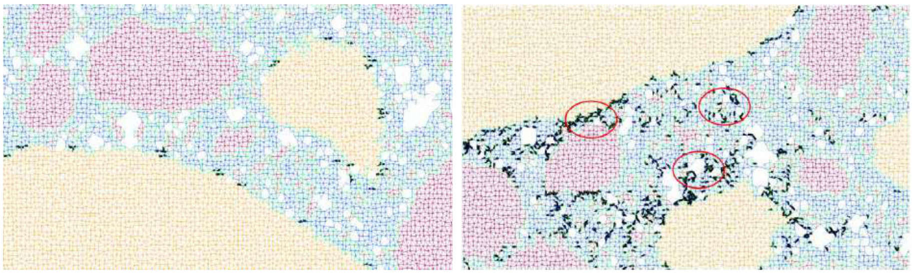

(a) Step 1000 (b) Final step

Fig. 13. Illustration of cracking development in the expansion model 3 at different analysis steps.

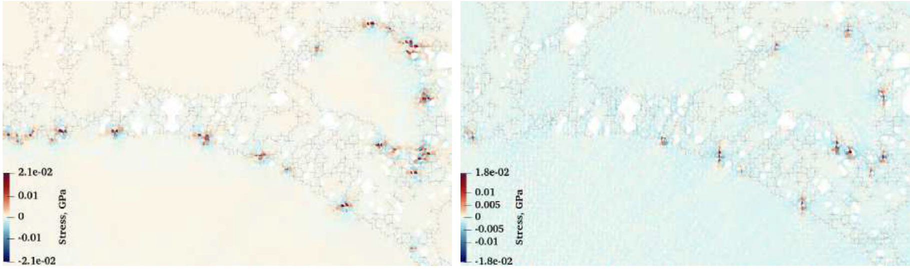

(a) Step 300 (b) Step 1000

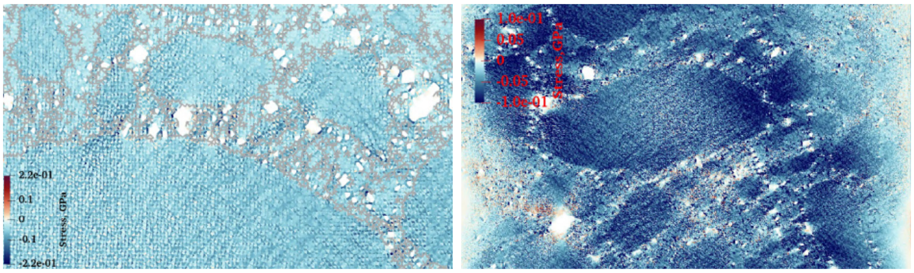

(c) Step 3000 (d) Final step

Fig. 14. Illustration of stress development in the expansion model 3 at different analysis steps. The black line represents the interfacial element.

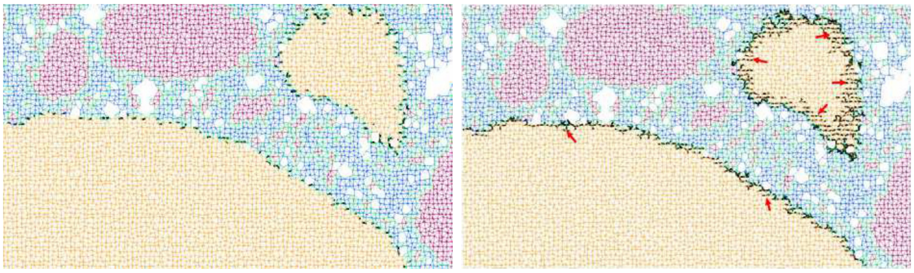

(a) Step 3000 (b) Step 9000

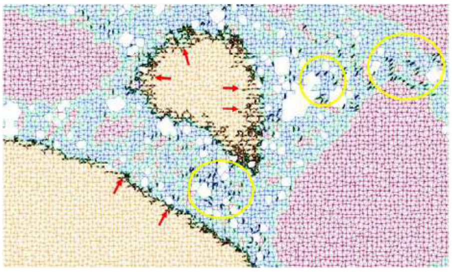

(c) Final step

Fig. 15. Illustration of cracking development in the expansion model 4 at different analysis steps.

reactive aggregate (Fig. 17(a) and Fig. 17(b)). With analysis step increasing, the stresses propagate around the expansive sites (inner rim and random sites) towards both the reactive aggregate and mortar matrix (Fig. 17(c)). Obviously, tensile stress propagates much further than the compressive stress. In the end, tensile stresses are distributed even in the whole big reactive aggregate as well as in the fine aggregate near the reactive aggregate (Fig. 17(d)) while compressive stress are mainly distributed at the expansive sites and inside the aggregate.

The above analyses indicate that in the expansion model 5 where the initial expansive sites are at the aggregate surface and randomly inside the aggregates with the ASR generated pressure in the range $[10^7, 10^8]$ Pa, cracking first appears in the reactive aggregate-cement paste interface, developing along the expansive site at the surface boundary of the reactive aggregate and extends into the reactive aggregate but near the boundary firstly. Cracking inside the reactive aggregate near the expansive sites happens later and finally cracking from the inside of the mortar matrix occurs. It

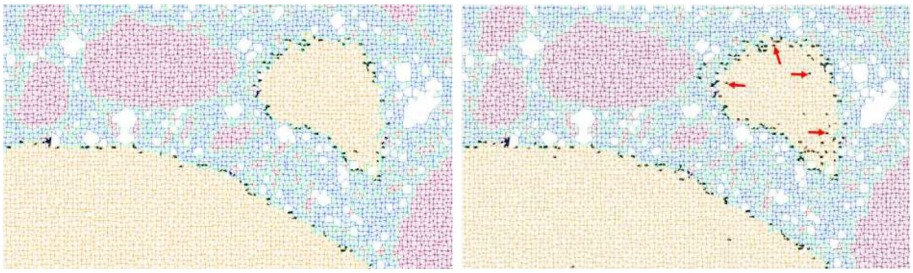

(a) Step 2000   (b) Step 3000

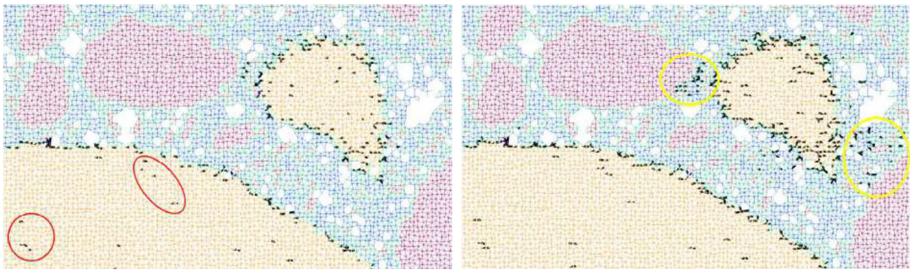

(c) Step 4000   (d) Final step

Fig. 16. Illustration of cracking development in the expansion model 5 at different analysis steps.

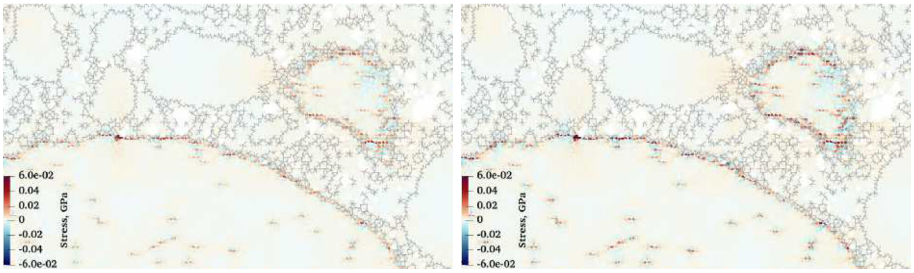

(a) Step 300   (b) Step 1000

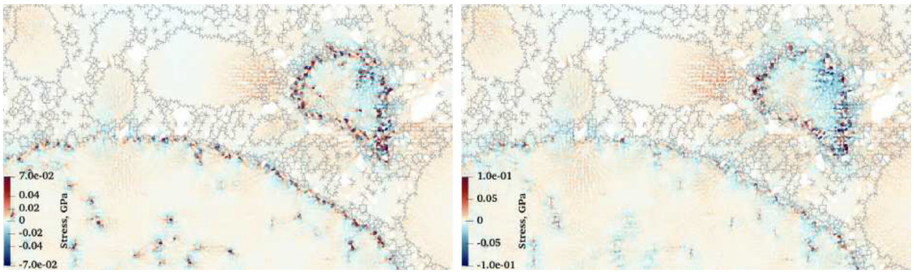

(c) Step 4000   (d) Final step

Fig. 17. Illustration of stress development in the expansion model 5 at different analysis steps. The black line represents the interfacial element.

is found that 6736 elements are broken due to the local tensile stress failure, and no element is broken due to compressive stress failure. From the stress distribution, a crack network can be noticed that connects the expansive sites inside the reactive aggregate and the mortar if the imposed expansive forces are increased.

3.5. Expansion model 6

In this expansion model, the expansive sites are distributed inside the outer rim, a layer with a distance of 1 mm to the surface of the reactive aggregate including the inner rim. The calculated pressure from $[D_{11}, D_{12}, D_{13}, D_{14}, D_{15}]$ (see Table 2) are taken. Due to high porosity resulting in a quick diffusion of ions into the aggregate, the calculated pressure is high and in the range $[10^7, 10^9]$ Pa with higher pressure inside the cement paste which can be explained by the higher alkali concentration in the cement paste. As introduced in Section 2.3.2, the expansive forces in the distance of 0.2 mm to 1 mm to the surface of the aggregate are taken as the linear decreasing value of the calculated expansive force in the inner rim.

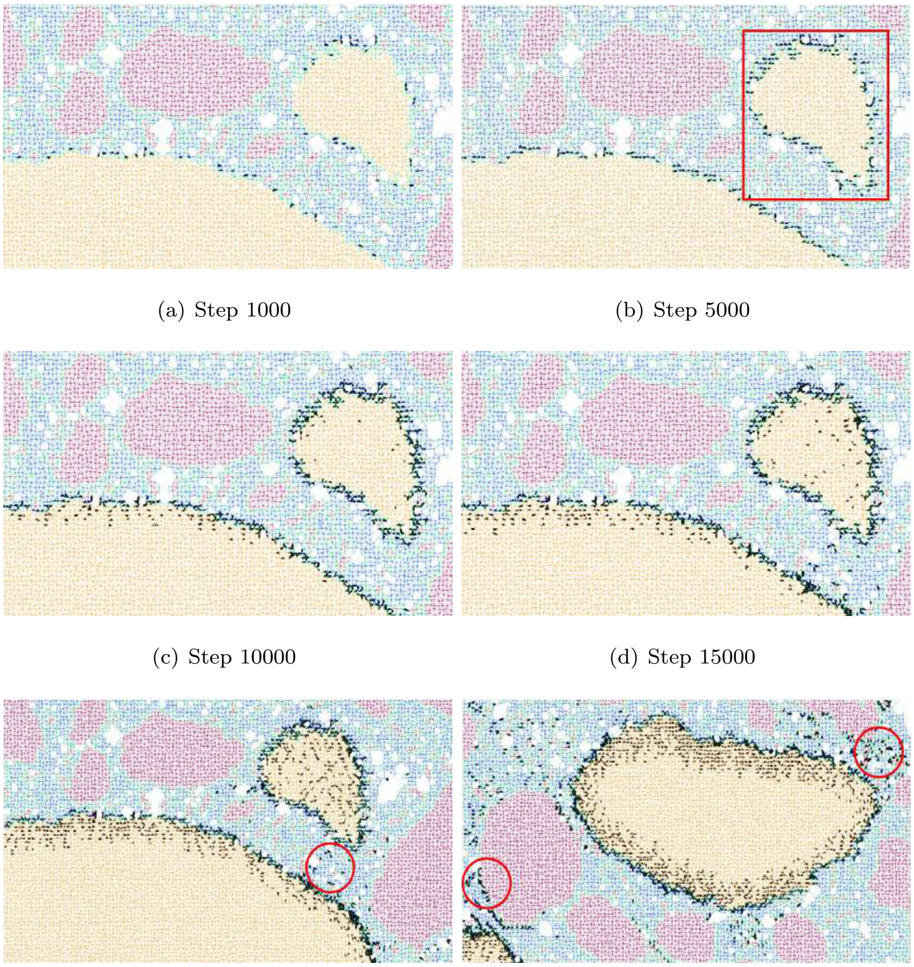
(a) Step 1000

(b) Step 5000

(c) Step 10000

(d) Step 15000

(e) Step 25000

(f) Final step

Fig. 18. Illustration of cracking development in the expansion model 6 at different analysis steps.

Due to a higher expansive force, the cracking pattern in this expansion model is different from the others and can be divided into four stages. In the first stage, initial cracks occur in the interfacial zone along the reactive aggregate surface as can be seen in Fig. 18(a). In the second stage, the cement paste near the interfacial zone in a limited distance begins to crack (see red square in Fig. 18(c)). This is because the initial expansive forces inside the cement paste are higher, resulting in a high tensile stress at/and near the expansive sites. In the third stage about after 10000 steps, massive cracks inside the reactive aggregate are observed. In the small reactive aggregate, the cracks are randomly distributed. But in the big reactive aggregate, the cracks are perpendicular to the surface within the expansive distance as shown by Fig. 18(d). In the final stage, cement paste begins to crack (Fig. 18(d)) and massive cracks inside cement paste are found in the end as shown by the red circle in Fig. 18(e). Some of close aggregates are connected by cracks.

The development of the stresses can be divided into three stages. In the first and second stage, stresses are generated in the interfacial elements as well as in the near cement paste elements as shown by Fig. 19(a) and Fig. 19(b). Then, the stresses become higher and propagate into the reactive aggregate as well as into the mortar matrix. But the highest stresses are still located in the interfacial zone. While when it comes to the third stage after 10000 steps, highest stresses occur in the expansive layers inside the big reactive aggregate and in the whole small reactive aggregate leading to the inner cracks (see Fig. 19(c) and Fig. 19(d)). In the final stage from 20000 steps to the final step, both tensile and compressive stresses propagates in the whole structure with the total stress kept in balance.

The above analyses indicate that in the expansion model 6 where the initial expansive sites are in the cement paste and a layer within a distance of 1 mm to the surface of the reactive aggregate and the ASR generated pressure is high which is in the range $[10^7, 10^9]$ Pa, cracking first appears in the aggregate-cement paste interface, developing along the expansive sites at the surface boundary of the reactive aggregate and then extends into the cement paste but in a very limited distance. Then cracking inside the aggregate perpendicular to the surface within the expansive distance occurs later and finally the mortar matrix is damaged. Cracks are formed mainly due to local tensile strength failure. It is found that 33717 elements are broken due to the local tensile stress failure, and 831 element are broken due to compressive stress failure.

4. Discussions

4.1. Summary of simulated cracking patterns at mesoscale

In this paper, the influence of the change of different expansive sites at mesoscale in concrete on the ASR induced expansion process caused by different exposure environment is evaluated via a mesoscale lattice fracture simulation model. Based on the chemical reaction simulation results in [17], six different expansive sites are

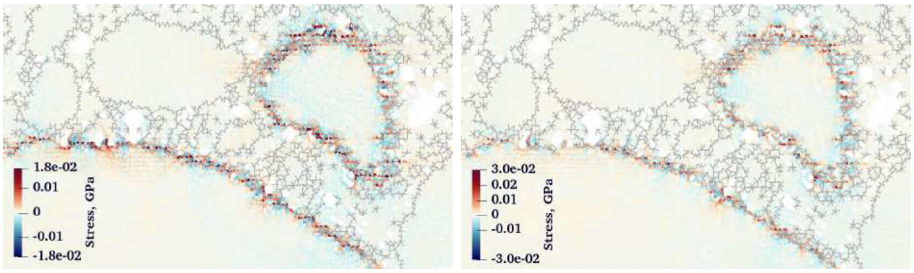

(a) Step 300 (b) Step 1000

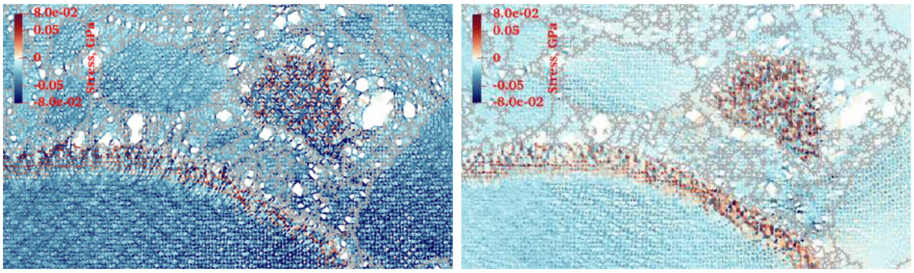

(c) Step 10000 (d) Step 15000

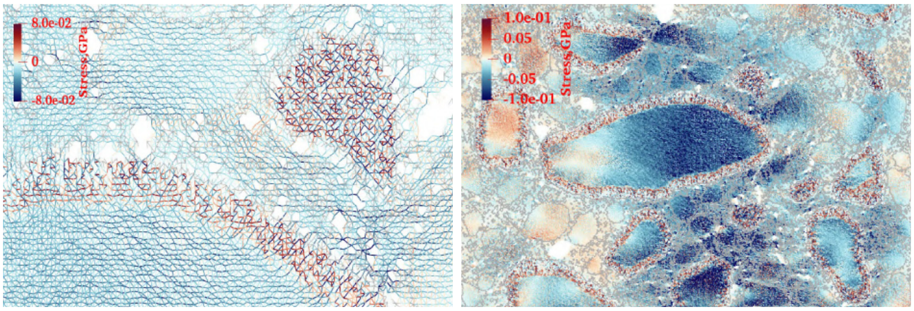

(e) Step 20000 (f) Final step

Fig. 19. Illustration of stress development in the expansion model 6 at different analysis steps. The black line represents the interfacial element.

considered: (1) in the reactive coarse aggregate surface within a distance of 0.1 mm; (2) in the cement paste connected to the reactive coarse aggregate within a distance of 0.1 mm; (3) in the reactive coarse aggregate surface within a distance of 0.1 mm and in the cement paste connected to the reactive coarse aggregate within a distance of 0.1 mm with a higher expansive pressure; (4) in the cement paste connected to the reactive coarse aggregate within a distance of 0.1 mm and in the reactive coarse aggregate surface within a distance of 0.1 mm with a higher expansive pressure; (5) in the reactive coarse aggregate surface within a distance of 0.1 mm and 1.25% random expansive sites inside the reactive aggregate; (6) in the reactive coarse aggregate surface within a distance of 0.1 mm and a expansive layer at the surface of the aggregate with a distance of 1 mm.

According to the simulation results in this work, the ASR-induced cracking process can be described based on four stages

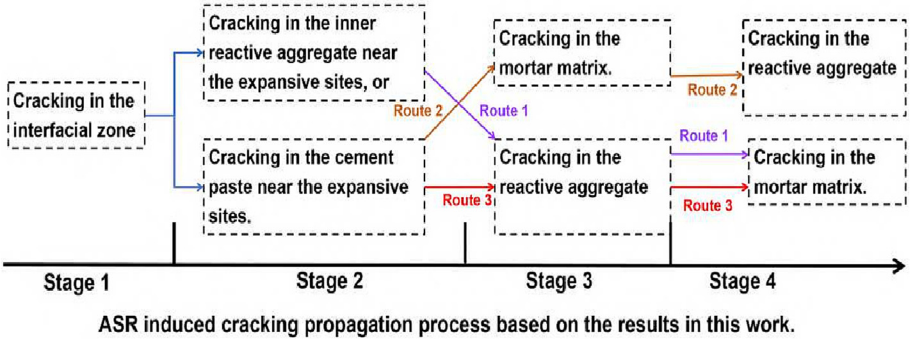

Fig. 20. Summary of the cracking routes based on the simulation results.

no matter where the expansive sites are distributed as shown in Fig. 20. In the first stage when the expansive forces are high enough to trigger cracking, part of elements in the interfacial zone, which includes the reactive aggregate surface, ITZ and the connected cement paste, are broken. In the second stage, cracking happens in the inner reactive aggregate or in the cement paste near the expansive sites depending on the comparative magnitude of the expansive forces inside the reactive aggregate and in the cement paste. In the third and fourth stage, the reactive aggregate matrix or the mortar matrix cracks. Three routes can be derived based on the simulation results as shown by different color arrows in Fig. 20. In route 1, cracking starts from the interfacial zone then in the inner reactive aggregate near the expansive sites, after that extends in the reactive aggregate matrix and finally in the mortar matrix. This is the case for the distribution pattern (1), (4) and (5) of the expansive sites that only locate inside the reactive aggregate (either at the surface or inside) or the expansive force inside the reactive aggregate is higher than that in the cement paste. In route 2 cracking starts from the interfacial zone then in the cement paste near the expansive sites, after that extends in the mortar matrix and finally in the reactive aggregate matrix. This is the case for the distribution pattern (2) and (3) of the expansive sites located only in the cement paste or in both aggregate surface and cement paste but when the expansive force in the cement paste is higher than that in the reactive aggregate surface. In route 3, cracking starts from the interfacial zone then in the cement paste near the expansive sites, after that extends in the reactive aggregate matrix and finally in the mortar matrix. This is the case for the distribution pattern (6) where the aggregate is highly porous so that ions can diffuse into the aggregate in a big distance so that ASR products are formed inside cement paste, ITZ as well inside aggregate. However, the expansive forces inside the cement paste are higher. The cracking is mainly caused by tensile strength failure. However, when the expansive force is very high in the cement paste, it is also possible the elements can be broken by the failure of compression strength in the later as shown by the expansion model 3.

Based on the chemical reaction simulation results at microscale, each cracking route at mesoscale is linked to specific aggregate properties and trigger environment. For the cracking route 1, the silica dissolution rate should be slow and the aggregate porosity should be low as shown in Fig. 21. This means that the reactive silica microstructural disorder degree should be small, and the reactive silica fraction should be low in the aggregate. The aggregate can contain some initial defects, but the temperature should be kept low (25 °C) so that the silica dissolution rate is not accelerated too much. For the cracking route 2, the silica dissolution rate should be high but the aggregate porosity should be low as shown in Fig. 21. For example, the aggregate can be highly-reactive volcanic glass or the aggregate is slowly-reactive one but the temperature is very high such as 80 °C or the silica distribution in the aggregate is heterogeneous and silica content at the surface of aggregate is very high so that reaction rims are formed locally around the aggregate. Initial defects should not occur in this case. If it happens, then the cracking route transfers to the route 3 as shown in Fig. 21 where ASR products should be found in ITZ, cement paste and aggregate. This route is only possible when the aggregate is highly porous. However, it should be borne in mind that the conclusive three cracking routes in this work cannot cover every realistic cracking pattern in the field but only give some insights to it.

4.2. Comparison with experimental observations

The above cracking patterns at mesoscale are simulated based on the chemical reaction simulation results at microscale with parameters being quantified. In the experimental observations, quantitative information about the aggregate such as the aggregate porosity, reactive silica fraction distribution in the aggregate or the exposure environment are generally not given. Instead, cracking patterns are normally identified according to the aggregate type (highly reactive or slowly reactive). In this section, some typical experimentally observed cracking will be compared with the simulation results and further discussed.

It is widely found that when the aggregate is highly-reactive such as volcanic igneous rock, ASR products are formed in the ITZ [3,4]. Fig. 22(a) from the work of [4] shows the cracking pattern with a highly-reactive aggregate. In the Fig. 22(a), left and right figure shows different reaction aggregates. By analysing thin-sections of the concrete sample at 30 days and 4 months, it was found that a reaction rim was found around some of the reactive aggregates and cracking was initiated in the interfacial zone and then propagates into the cement paste. No cracking inside the aggregate was found. According to the simulation results in this study, this is consistent with the simulated pattern in the expansion model 2 as shown in

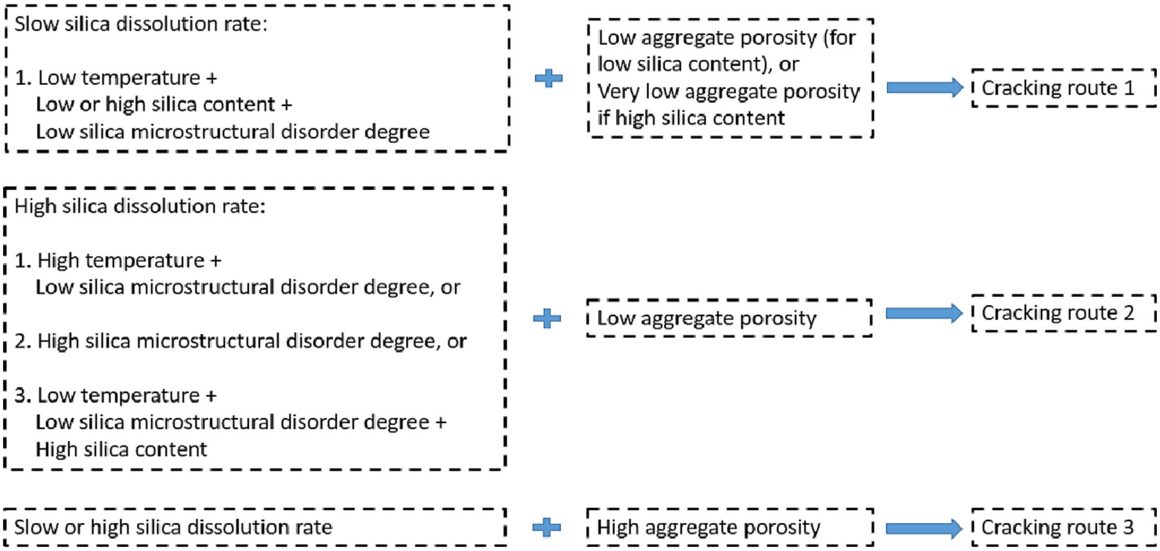

Fig. 21. A diagram showing the link between the chemical reaction to cracking routes based on the simulation results in [24] and this work.

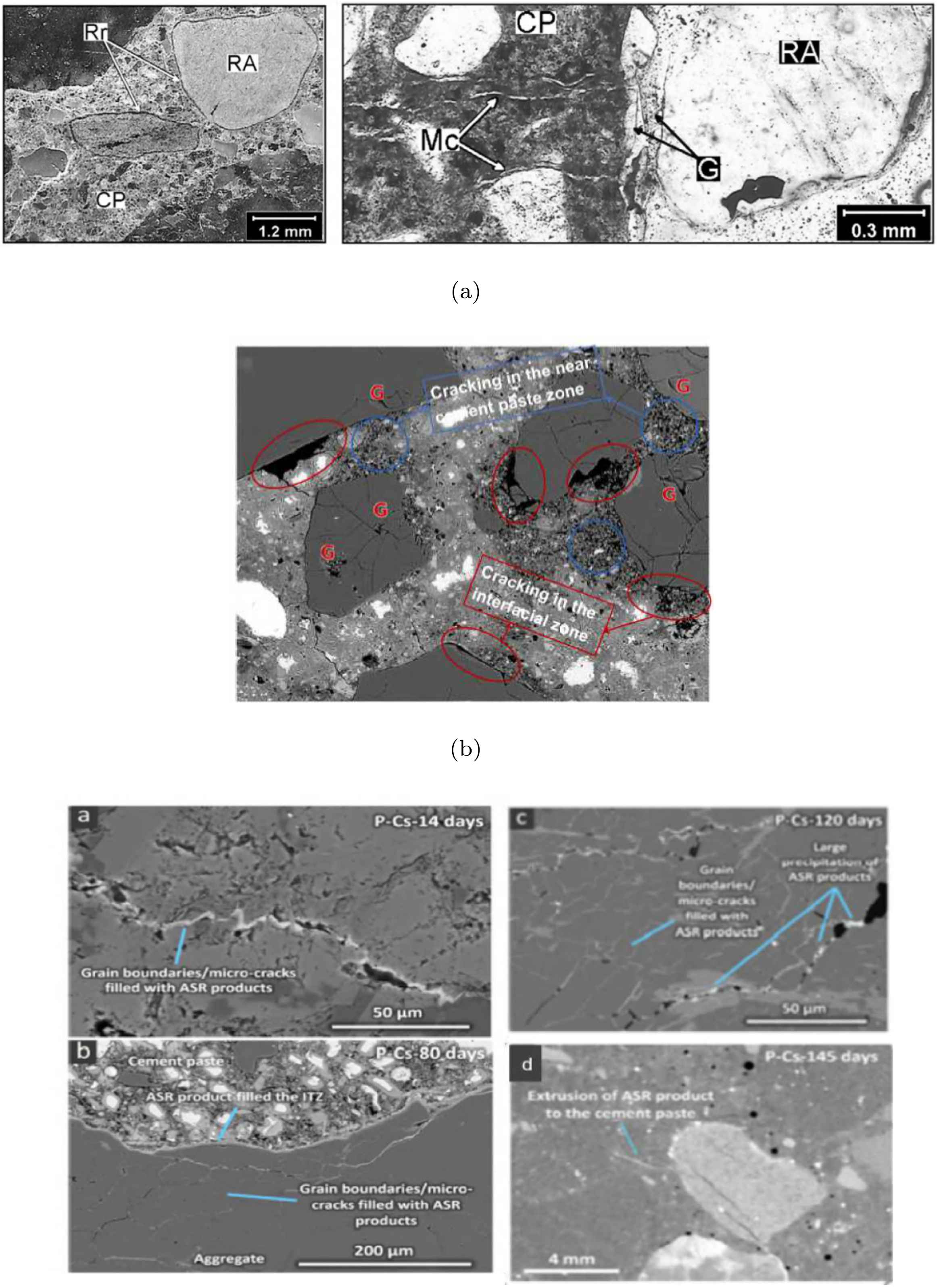

(a)

(b)

(c)

Fig. 22. (**a**): Cracking patterns in concrete with highly-reactive aggregate from [4]. Left and right figure shows different aggregates. RA: highly reactive aggregate. Rr: reaction rim, CP: cement paste, Mc: microcrack, G:gel; (**b**): Observed cracking pattern in a mortar sample with mixed mineralogy aggregates at 40 °C after ten weeks modified from [12], G means gel packets; (**c**): ASR induced crack-temporal evolution in concrete with low reactive aggregate from [7]. P-Cs: P-aggregate with Cs added in the concrete sample. Cs: caesium.

Fig. 11. The simulation results in this study also provide more information about the conditions for this kind of cracking pattern to happen: the reactive aggregate either contains no initial defects or the porosity is low and the aggregate is so reactive that most of the ions are consumed before it can further diffuse into the aggregate. Besides, the formation of a reaction rim means that the silica distribution in the aggregate is very homogeneous, which is usually the case for the highly reactive aggregate [15].

In 2010, Dunant and Scrivener [12] proposed a model based on the experimental observations at mesoscale which claims that crack initiation is within the reactive aggregates with mixed mineralogy (with both highly-reactive and slowly-reactive silica) as shown in Fig. 22(b). The reactivity of the aggregate is not specified in their work, but according to the work of [3], this kind of aggregate belongs to the low to middle-reactive aggregate and the initial expansive sites are inside the aggregate [3]. However, it can be seen from Fig. 22(b) that after ten weeks, except for the cracks inside the aggregates and connecting aggregates, it is obvious that some reactive aggregates ares totally debonded or partially debonded from the cement paste as shown by the red circle. Damage of the cement paste zone near the reactive aggregate is also very apparent as shown by the blue circle. The final cracking pattern shown in Fig. 22(b) is comparable to the simulated cracking pattern from the expansion model 5 in this work as shown in Fig. 16, in which the expansive sites are distributed at the reactive surface and inside the aggregate due to the initial defects. One difference is that a cracking network inside the reactive aggregate is not formed yet in the expansion model 5 and the damage of cement paste zone near the reactive aggregate zone is missing as well in the simulated cracking pattern. These discrepancies can be explained by the magnitude of the expansive force in the expansion model 5 that it is not high enough to generate a crack network and crack the near cement paste. The distribution of the produced stresses in the aggregate and in the cement paste near the aggregate in Fig. 17 confirms this statement. The specific cracking propagation process is not revealed in their work, but it is reasonable to apply the cracking route 3 (Fig. 20) to explain the development of the cracking pattern shown in Fig. 22(b) based on the applied aggregate and temperature. Ions firstly act with the silica located at the surface of the aggregate, resulting in ASR products in the interfacial zone. A reaction rim is missing probably because the reactive silica is dispersed distributed at the aggregate surface. At the same time, ions can diffuse into the inside of the aggregate through the initial defects to react with the silica and produce gel pocket there. But the ion concentration must have decreased due to the consumption and the uneasy diffusion path. As a result, cracking is most likely to initiate from the local interfacial zone since the mechanical properties there are lower than that of the aggregate matrix. Then the aggregate matrix cracks and propagates towards the cement paste and is able to connect two close reactive aggregate. At the same time, the expansion inside the aggregate is possible to further intensify the debonding of the aggregate from the cement paste as well as the cracking in the near cement paste zone to make it more obvious.

Recently, by using X-ray micro-tomography, Shakoorioskooie et al. [7] have studied the spatial–temporal evolution of ASR products and cracks at mesoscale in concrete samples with low-middle reactive aggregate at a temperature of 40 °C. In their, caesium (Cs), which can be incorporated into ASR products as an aklai, is added in the concrete mix to serve as a X-ray attenuation contrast enhancer between ASR products and the other material phases. Their results as shown in Fig. 22(b) indicate that cracks with ASR products appear firstly in the aggregates, close to the interface with the cement paste. They propagate afterwards towards the aggregates interior. Some products are then extruded for several mm into air voids and cracks in the cement paste. This route is the same as the simulated cracking route 1 in the expansion model 5. This means that the initial ASR products are mainly produced inside the aggregate (at the surface and/or interior). But a total debonding of the aggregate in Fig. 22(b) is missing which means the distribution of the reactive silica at the surface is heterogeneous. The simulation results in this study indicate that the silica fraction in the used aggregate in [7] is very low and dispersedly distributed at the surface and there are initial defects inside the aggregate. However, this cracking route can also happen even if there are no initial defects inside the aggregate as found from the expansion model 1 as long as the aggregate is not highly reactive with a low silica fraction and the porosity is low as well as the temperature is not very high.

4.3. Insights from this work

There is a long-term discussion about where the cracks induced by ASR are initiated in concrete. In the beginning, two cracking patterns are generalized according to the reactivity of the aggregate: from the inside of the aggregate by the formation of gel in the slowly-reactive aggregate [3,11,4,12] and from the cement paste by the formation of a reaction product rim in the ITZ around the high-reactive aggregate [3,2,4]. It is very soon reported that even with a highly reactive aggregate, cracking can start from the inside of the aggregate due to the initial defects inside the aggregate [6]. Recently, Miura et al. [15] have introduced the distribution of the silica fraction as a factor determining where the cracking origin is. They assumed that the silica is homogeneously distributed in the high-reactive aggregate, resulting in the formation of a reaction rim. While the low-reactive aggregate prefers the formation of gel pockets inside the aggregate.

The study in this work has shown that the real situation is much more complicated so that it cannot be predicted simply by the aggregate type since ASR is influenced not only by the reactivity of the aggregate, but also by other factors such as temperature, aggregate porosity, reactive silica distribution etc. It is possible that different cracking origins can occur in the same aggregate. For example, if the aggregate is slowly-reactive but the silica distribution is very heterogeneous at the surface resulting a local concentration of silica at some locations, then it is possible that the reaction products will be formed in the ITZ close to those locations while inside the aggregate at other locations where the silica fraction is low. The porosity and the initial defects also play a significant role in determining the cracking origins. ASR products will be formed inside the aggregate no matter how reactive it is if the aggregate porosity is high or there are some initial defects which is the general situation. Rather than assuming the location of the expansive sites inside the aggregate or inside the cement paste, which is applied in the most of cracking simulation model [14,15], it is more realistic to connect the chemical reaction at a low spatial scale and the physical response at a high spatial scale by considering as much influential factors as possible, which is the significance of this work.

5. Limitations

The work in this study has linked the chemical reaction of ASR at microscale and its physical response-cracking development at mesoscale. It has shed some light on better understanding ASR and better predicting the induced cracking propagation process. However, there are also some limitations of the work. Firstly, the simulation structure size limitation due to computer resources at microscale has limited the minimum crack width (100 μm in this work) at mesoscale, which means that smaller cracks at a lower spatial scale are not captured. Besides, the heterogeneity of the mechanical properties of the aggregate, due to the heterogeneous porosity distribution, is not considered either. The observed cracking patterns would not be affected as the mechanical properties of aggregate is much higher than that of ITZ and cement paste. However, it may affect the cracking development inside the aggregate as well as the magnitude of the local critical expansive force to crack the aggregate. What's more, limited by the adoption of some untested parameters, such as the mechanical properties of ITZ, cement paste and aggregate in the 2D structure as well as the compressibility of ASR products in this work, quantitative data such as the mechanical property change of the structure, number of cracks cannot be evaluated. Future works can be done to further build the relationship between the mechanical property changes of the structure induced by ASR such as the elastic modulus and tensile strength at mesoscale, and the chemical reaction degree as well as the chemical reaction process at microscale. To achieve this, the mechanical properties of ITZ, cement paste and aggregate should be calibrated as well as the compressibility of the ASR products. Further more, the external constraints on the concrete structures should also be considered as it has great influence on the critical expansion forces to crack the surrounding materials. More importantly, it should be borne in mind that the cracking is not coupled in the 3D reactive transport model at microscale, so that only the physical response in the early stage of ASR can be captured at mesoscale in this work.

6. Summary

In this paper, we have upscaled our chemical reaction simulation results as presented in [17] from microscale to mesoscale to build a bridge between the chemical reaction of ASR and the physical response via a lattice fracture model. A 2D slice from a structure of $40 \times 40 \times 40$ mm^3 with irregular reactive coarse aggregate, fine aggregate, air voids and cement paste is selected and meshed in the model to represent the concrete. The chemical reaction simulation results in a 3D domain composed by cement paste and aggregate are then used as a basis to calculate the ASR induced expansive forces. Six different expansion models are then proposed to investigate the influence of different initial expansive sites on the ASR cracking propagation process. The simulation results are synthesized and compared with the experimental observations. The main findings are listed as follows.

1) Assuming that reactive silica is distributed at the surface of the reactive aggregate, the cracking propagation process induced by ASR is divided into four stages. In the first stage cracking always starts from the damage in the interfacial zone. In the second stage, aggregate or cement paste near the expansive site will be broken depending on the comparative expansive force magnitude. In the third and final stage, the cracking extends firstly towards aggregate interior then towards mortar matrix or firstly towards mortar matrix then towards aggregate interior. Consequently, three typical cracking routes at mesoscale are derived based on the simulated cracking propagation process and each cracking route is linked with the chemical reaction mechanism at microscale. More specifically, the trigger conditions for each cracking route are given as specificly as possible based on the simulation results at microscale. Among them, the influential factors that can greatly affect the silica dissolution rate and the aggregate porosity are the most decisive factors. A slow silica dissolution rate (low temperature and small silica fraction and low silica microstructural disorder) and small aggregate porosity or with initial defects inside the aggregate probably will result in the cracking route 1 in which ASR products will be formed inside the aggregate and cracking starts from the interfacial zone and extends towards the aggregate interior and then propagates into the cement paste. While a high silica dissolution rate (high temperature or high silica microstructural disorder) and low aggregate porosity will results in the cracking route 2 in which cracking originated from the interfacial zone and then extends to the mortar matrix and finally inside the aggregate. If the aggregate is highly porous, then ASR products are distributed globally resulting in the cracking route 3 in which cracking initiates from the interfacial zone and then in the near cement paste zone making the aggregate debonded. After that, perpendicular cracks inside the aggregate to the aggregate surface will occur and finally propagate into the mortar matrix.
2) The proposed cracking routes are comparable with the experimental observations. It is time-consuming to conduct experiments to obtain the spatial–temporal evolution of ASR induced cracking process for a specific structure. The results in this work can provide some insights to predict the cracking process for the newly-built structure given the aggregate properties and exposed environment are known. The results can also provide possible detailed explanation for the observed cracking patterns and even the environmental exposing history for the field concrete.
3) The cracking origins induced by ASR cannot be predicted simply by the aggregate type (aggregate interior for slowly-reactive aggregate and reaction rim around the aggregate for highly-reactive aggregate) since ASR is influenced not only by the reactivity of the aggregate, but also other factors such as aggregate porosity, reactive silica distribution and exposed temperature etc. It is possible that different cracking origins can occur in the same aggregate due to the heterogeneous reactive silica distribution and different exposed environment thus leading to complicated mixed cracking routes.
4) The adoption of a high temperature (80 °C) in the accelerated mortar test [35] tends to change the cracking process from the aggregate interior to the cement paste when a slowly-reactive aggregate is used, thus giving misleading estimation of the mechanical change of the structure. A more representative testing result of the concrete prism test [36] is confirmed from another perspective in this work.

Declaration of Competing Interest

The authors declare that they have no known competing financial interests or personal relationships that could have appeared to influence the work reported in this paper.

Acknowledgement

The authors would like to thank the China Scholarship Council (CSC) for the financial support to the first author and the second author.

References

[1] J. Bérard, R. Roux, La viabilité des bétons du québec: le rôle des granulats, Can. J. Civ. Eng. 13 (1986) 12–24.

[2] T. Ichikawa, M. Miura, Modified model of alkali–silica reaction, Cem. Concr. Res. 37 (2007) 1291–1297.

[3] J. Ponce, O.R. Batic, Different manifestations of the alkali–silica reaction in concrete according to the reaction kinetics of the reactive aggregate, Cem. Concr. Res. 36 (2006) 1148–1156.

[4] G. Giaccio, R. Zerbino, J. Ponce, O.R. Batic, Mechanical behavior of concretes damaged by alkali–silica reaction, Cem. Concr. Res. 38 (2008) 993–1004.

[5] C. Dunant, Experimental and modelling study of the alkali–silica reaction in concrete (Technical Report), EPFL, 2009.

[6] F. Rajabipour, H. Maraghechi, G. Fischer, Investigating the alkali–silica reaction of recycled glass aggregates in concrete materials, J. Mater. Civ. Eng. 22 (2010) 1201–1208.

[7] M. Shakoorioskooie, M. Griffa, A. Leemann, R. Zboray, P. Lura, Alkali–silica reaction products and cracks: X-ray micro-tomography-based analysis of their spatial-temporal evolution at a mesoscale, Cem. Concr. Res. 150 (2021) 106593.

[8] G.W. Groves, X. Zhang, A dilatation model for the expansion of silica glass/OPC mortars, Cem. Concr. Res. 20 (1990) 453–460.

[9] Y. Furusawa, H. Ohga, T. Uomoto, Analytical study concerning prediction of concrete expansion due to alkali–silica reaction, Special Publication 145 (1994) 757–780.

[10] Z.P. Baant, A. Steffens, Mathematical model for kinetics of alkali–silica reaction in concrete, Cem. Concr. Res. 30 (2000) 419–428.

[11] M.B. Haha, E. Gallucci, A. Guidoum, K.L. Scrivener, Relation of expansion due to alkali silica reaction to the degree of reaction measured by SEM image analysis, Cem. Concr. Res. 37 (2007) 1206–1214.

[12] C.F. Dunant, K.L. Scrivener, Micro–mechanical modelling of alkali–silica–reaction induced degradation using the AMIE framework, Cem. Concr. Res. 40 (2010) 517–525.

[13] Y. Wang, Y. Meng, P. Jiradilok, K. Matsumoto, K. Nagai, S. Asamoto, Expansive cracking and compressive failure simulations of ASR and DEF damaged concrete using a mesoscale discrete model, Cem. Concr. Compos. 104 (2019) 103404.

[14] T. Iskhakov, J.J. Timothy, G. Meschke, Expansion and deterioration of concrete due to ASR: micromechanical modeling and analysis, Cem. Concr. Res. 115 (2019) 507–518.

[15] T. Miura, S. Multon, Y. Kawabata, Influence of the distribution of expansive sites in aggregates on microscopic damage caused by alkali–silica reaction: insights into the mechanical origin of expansion, Cem. Concr. Res. 142 (2021) 106355.

[16] L. Sanchez, B. Fournier, M. Jolin, J. Duchesne, Reliable quantification of AAR damage through assessment of the damage rating index (DRI), Cem. Concr. Res. 67 (2015) 74–92.

[17] X. Qiu, J. Chen, G. Ye, G. De Schutter, Insights in the chemical fundamentals of asr and the role of calcium in the early stage based on a 3d reactive transport model, Cem. Concr. Res. (2022).

[18] Z.W. Qian, Multiscale modeling of fracture processes in cementitious materials, Ph.D. thesis, Delft University of Technology, Delft, The Netherlands, 2012.

[19] P. Gao, Y. Chen, H. Huang, Z. Qian, E. Schlangen, J. Wei, Q. Yu, Effect of relative humidity on drying-induced damage in concrete: a comparative study of digital image correlation and lattice modelling, Mater. Design 196 (2020) 109128.

[20] X. Ma, E. Schlangen, O. Çopuroğlu, Experimental and numerical study on mechanical properties of cement paste pipes subjected to uniaxial tensile loading, Theoret. Appl. Fract. Mech. 103 (2019) 102296.

[21] J. Chen, G. Ye, A lattice boltzmann single component model for simulation of the autogenous self-healing caused by further hydration in cementitious material at mesoscale, Cem. Concr. Res. 123 (2019) 105782.

[22] J.J. Kim, T. Fan, M.M. Reda Taha, A homogenization approach for uncertainty quantification of deflection in reinforced concrete beams considering microstructural variability, Struct. Eng. Mech. 38 (2011) 503.

[23] E.J. Garboczi, D.P. Bentz, Computer simulation and percolation theory applied to concrete, Annual Reviews of Computational Physics VII 85 (1999).

[24] X. Qiu, J. Chen, M. Deprez, V. Cnudde, G. Ye, G.D. Schutter, 3D microstructure simulation of reactive aggregate in concrete from 2D images as the basis for ASR simulation, Materials 14 (2021) 2908.

[25] H. Zhang, B. Šavija, S. Chaves Figueiredo, M. Lukovic, E. Schlangen, Microscale testing and modelling of cement paste as basis for multi-scale modelling, Materials 9 (2016) 907.

[26] M. Luković, B. Šavija, E. Schlangen, G. Ye, K. Van Breugel, A 3D lattice modelling study of drying shrinkage damage in concrete repair systems, Materials 9 (2016) 575.

[27] H. Zhang, Y. Xu, Y. Gan, Z. Chang, E. Schlangen, B. Šavija, Combined experimental and numerical study of uniaxial compression failure of hardened cement paste at micrometre length scale, Cem. Concr. Res. 126 (2019) 105925.

[28] H. Zhang, Y. Gan, Y. Xu, S. Zhang, E. Schlangen, B. Šavija, Experimentally informed fracture modelling of interfacial transition zone at micro-scale, Cem. Concr. Compos. 104 (2019) 103383.

[29] H. Zhang, Y. Xu, Y. Gan, E. Schlangen, B. Šavija, Experimentally validated mesoscale fracture modelling of mortar using output from micromechanical models, Cem. Concr. Compos. 110 (2020) 103567.

[30] X. Qiu, J. Chen, G. Ye, G. De Schutter, A 3D reactive transport model for simulation of the chemical reaction process of ASR at microscale, Cem. Concr. Res. 151 (2022) 106640.

[31] Z. Chang, H. Zhang, E. Schlangen, B. Šavija, Lattice fracture model for concrete fracture revisited: Calibration and validation, Appl. Sci. 10 (2020) 4822.

[32] M. Berra, G. Faggiani, T. Mangialardi, A. Paolini, Influence of stress restraint on the expansive behaviour of concrete affected by alkali–silica reaction, Cem. Concr. Res. 40 (2010) 1403–1409.

[33] J. Liaudat, I. Carol, C.M. López, V.E. Saouma, ASR expansions in concrete under triaxial confinement, Cem. Concr. Compos. 86 (2018) 160–170.

[34] H. Kagimoto, Y. Yasuda, M. Kawamura, ASR expansion, expansive pressure and cracking in concrete prisms under various degrees of restraint, Cem. Concr. Res. 59 (2014) 1–15.

[35] ASTM, Standard test method for potential alkali reactivity of aggregates (mortar-bar method), ASTM C 1260-01 (2007).

[36] ASTM, Standard test method for determination of length change of concrete due to alkali–silica reaction, ASTM C 1293-01 (2008).